ABSTRACT

Title of Thesis:	GROWTH AND STABILIZATION OF AG AND NI NANOCLUSTERS WITHIN A POLYMER MATRIX VIA AEROSOL SPRAY PYROLYSIS
	Michelangelo Romano, Master of Science, 2017
Thesis Directed By:	Professor Michael R. Zachariah Department of Chemistry and Biochemistry Department of Chemical and Biomolecular Engineering

Metal nanoclusters exhibiting enhanced properties are inherently unstable because of their high specific surface area. This work investigates how the undesirable agglomeration of these nanostructures can be circumvented by incorporating them into a polymer matrix. Using aerosol spray pyrolysis (ASP), Ag and Ni nanoclusters less than 20 nm in diameter have been synthesized by growing and trapping them within polyvinylpyrrolidone (PVP), polyethylene glycol (PEG), and polyethylene oxide (PEO). Experimental process variables including the polymer system's molecular weight, the temperature of the tube furnace reactor, the carrier gas flow rate, and the metal salt concentration within the ASP precursor solution have been studied to understand which parameters govern nanocluster formation and growth. Having analyzed the correlations that exist between these parameters and the size distribution of the Ag and Ni nanoclusters, a qualitative model is proposed that identifies which primary mechanisms underlie the formation of metal nanoclusters within a polymer matrix.

GROWTH AND STABILIZATION OF AG AND NI NANOCLUSTERS WITHIN A POLYMER MATRIX VIA AEROSOL SPRAY PYROLYSIS

by

Michelangelo Romano

Thesis submitted to the Faculty of the Graduate School of the
University of Maryland, College Park, in partial fulfillment
of the requirements for the degree of
Master of Science
2017

Advisory Committee:
Professor Michael R. Zachariah, Chair
Professor Bryan Eichhorn
Professor Raymond Phaneuf

Acknowledgements

I would like to express my most sincere gratitude to all of the wonderful students, faculty, and staff who have supported my graduate studies at UMD. Firstly, I would like to acknowledge my advisor, Dr. Michael Zachariah, whose mentorship and guidance has been indispensable for my professional development. Secondly, I would like to recognize the immense support of my student colleagues who were always readily available to offer assistance with my research. Lastly, I would like to thank all of the faculty and staff members within the MSE department who have supported me in my coursework and enriched my experience as a graduate student at UMD.

Table of Contents

List of Tables

List of Figures

Chapter 1: Introduction and Background

1.1 Polymer Nanocomposites

Metal nanoclusters less than 20 nm in diameter have been reported to exhibit enhanced properties for electronic, optical, and biomedical applications.[1–3] To synthesize these extremely small nanoparticles, however, particle-particle interactions must be minimized during synthesis since the high specific surface area of such nanoclusters can lead to the undesired formation of microscale agglomerates. This can be achieved by depositing and trapping nanoparticles within a polymer matrix. The ligands and organic linkers within a polymer can be used to strengthen the bonding between the inorganic nanoparticles and the organic matrix, ultimately preventing nanoparticle agglomeration.

These hybrid materials are referred to as polymer nanocomposites and their synthesis has been investigated with ex situ and in situ nanoparticle generation techniques (as illustrated in Figure 1-1).[4] Ex situ nanoparticle generation techniques rely on thermal or mechanical processes such as nanolithography, laser ablation, and ball-milling to generate nanoparticles that can later be introduced within a polymer. This approach allows one to control the shape and size of nanoparticles being incorporated within the polymer. Unfortunately, many nanoparticles generated using ex situ techniques require the use of capping agents or surfactants to inhibit nanoparticle agglomeration. The residual adsorption of these chemical reagents on the surface of the nanoparticles has the potential to render them incompatible with a polymer matrix. While this issue can be mitigated using functional group grafting or strategic ligand exchanges, the morphology of the synthesized nanoparticles might be

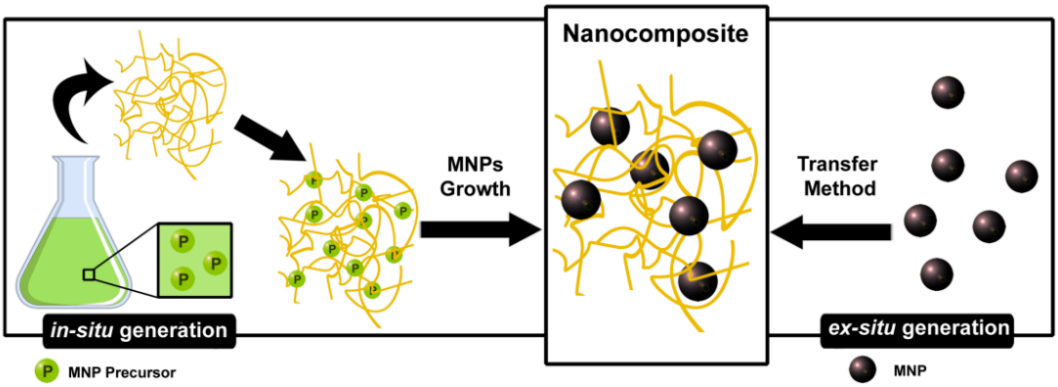

Figure 1-1: Schematic illustration comparing ex situ and in situ nanoparticle generation techniques for synthesizing polymer nanocomposites. Reprinted from Chapter 3 of B. Domènech, J. Bastos-Arrieta, A. Alonso, J. Macanás, M. Muñoz and D. N. Muraviev (2012). Bifunctional Polymer-Metal Nanocomposite Ion Exchange Materials, Ion Exchange Technologies, Prof. A. Kilislioglu (Ed.). Published by InTech under CC BY 3.0 license. Available from http://dx.doi.org/10.5772/51579. Full terms found at https://creativecommons.org/licenses/by/3.0/legalcode.[4]

substantially altered. Alternatively, in situ nanoparticle generation techniques refer to the formation of nanoparticles directly within a polymer matrix. This single-step polymer nanocomposite fabrication method incorporates metal-ion precursors into a polymer matrix. In essence, the polymer functions as a soft template for guiding the nucleation and growth of the inorganic nanoparticles. This method eliminates the need for surfactants and capping agents, yielding a higher nanoparticle number density and a more uniform nanoparticle distribution throughout the polymer matrix.

Harnessing the intriguing properties of nanoclusters by encapsulating them within polymer matrices can also lead to innovative hybrid materials. Fundamentally, the polymer serves as a framework for stabilizing nanoparticles. However, the strategic combination of nanoparticles and specific types of polymers can yield enhanced functionality for these composite materials. In many cases, nanoparticles incorporated within polymers have been demonstrated to increase the system's mechanical stability.[5–7] Other synergistic effects have augmented the composite

material's electrical and optical properties. For example, the introduction of metal nanoparticles into organic photovoltaics has led to improved efficiencies, stemming from the enhanced light absorption and scattering properties of the incorporated nanoparticles.[8] Furthermore, nanoparticles embedded within electrically conductive polymers (e.g., polyaniline) have the potential to serve as innovative composite materials for electrodes within Li-ion batteries.[9]

The properties of polymer nanocomposites can be strategically tailored for specific applications. As illustrated in Figure 1-2, there are many possible interactions that can occur between inorganic nanoparticles and the surrounding polymer matrix.[10] By modifying the polymer system's degree of polymerization, crystallinity, and/or tacticity, various types of composite structures can be formed that alter the size, arrangement, spacing, and distribution of nanoparticles encapsulated within the polymer medium. Innovative ex situ and in situ techniques that investigate how to strategically manipulate these parameters for designing hybrid composite materials have propelled polymer nanocomposites to the forefront of materials research.

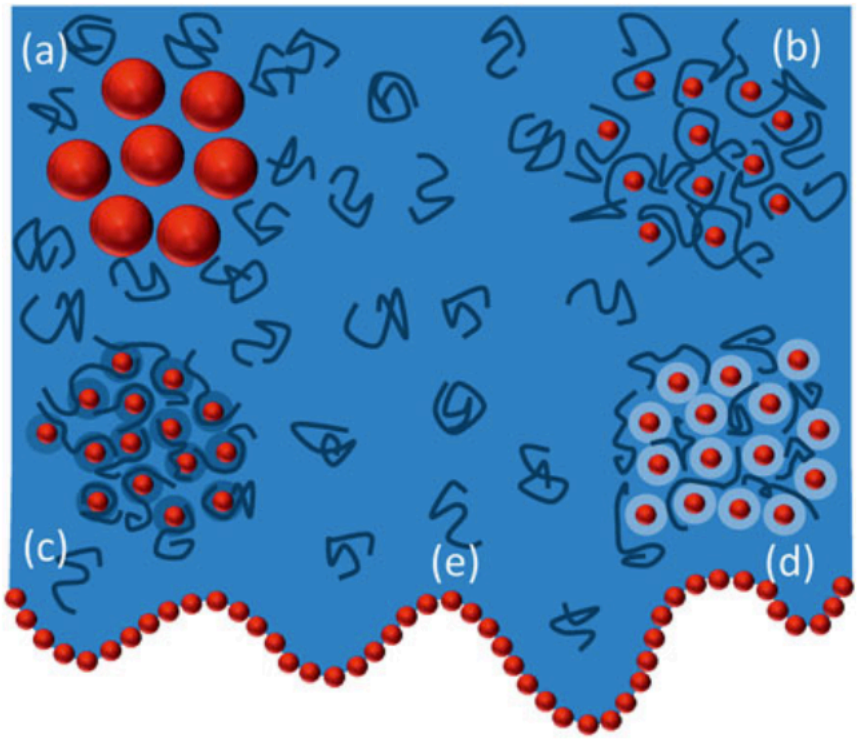

Figure 1-2: Illustration of the possible interactions that can occur between inorganic nanoparticles and polymer chains. **(a)** Nanoparticles larger than the polymer chains attracted together by depletion forces. **(b)** Small nanoparticles spaced apart by interpenetrating polymer chains. **(c)** Polymer nanocomposite system with favorable interactions resulting in a lower free volume near the particle surface. **(d)** Polymer nanocomposite system with unfavorable interactions resulting in a higher free volume near the particle surface. **(e)** Nanoparticles functioning as surfactants to stabilize high surface area polymer structures. Reprinted from Firestone, M. A., Hayden, S. C. & Huber, D. L. Greater than the sum: Synergy and emergent properties in nanoparticle–polymer composites. MRS Bulletin, Volume 40, Issue 9, 760–767 (2015). Reproduced with permission.[10]

1.2 Relevant Research

The synthesis of polymer nanocomposite materials using ex situ nanoparticle generation techniques has been investigated to exploit the properties of prefabricated nanoparticles with particular morphologies. Bridging the gap between these inorganic nanostructures and organic macromolecules, however, has been far from trivial. One approach for stabilizing nanoparticles has been to incorporate them into a polymer using miniemulsions. These emulsions are colloidal mixtures comprised of two

immiscible liquids effectively stabilized by an amphiphilic surfactant. The concentration of surfactant within the emulsion will determine if coalescence or micellar nucleation of the dispersed phase might occur.[11] Upon incorporating a particular type of monomer and inorganic nanoparticle within the emulsion, a polymerization process can be initiated to synthesize polymer droplets that encapsulate and stabilize the nanoparticles. Difficulties with monomer and nanoparticle aggregation stemming from the surfactant concentration, however, have prompted the need for chemically modifying the surface of the nanoparticles.

Capping the surface of nanoclusters with strategic functional groups has facilitated the synthesis of polymer nanocomposite materials using ex situ synthesis techniques. With this miniemulsion approach, Joumaa et al. have demonstrated that trioctylphosphine oxide coated or vinyl-functionalized CdS/ZnS core-shell quantum dots can be successfully incorporated into polystyrene droplets.[12] Further work by Luo et al. has shown that strategic functionalization of the surface of inorganic nanoparticles can be used to control the clustering and location of nanoparticles within block co-polymer droplets.[13] In their work, Au nanoparticles originally stabilized with dodecanethial (DT) during synthesis were subjected to a ligand exchange process that resulted in a fraction of the DT ligands being replaced with 11-mercapto-1-undecanol (MUL) ligands. Upon varying the MUL concentration used within the ligand exchange process, the ratio of DT ligands (hydrophobic) to MUL ligands (hydrophilic) could be controlled. When the surface-modified Au nanoparticles were encapsulated within polystyrene (inner) and polyacrylic (outer) copolymer core-shell droplets, their aggregation patterns within the droplets changed

substantially. Increasing the fraction of MUL ligands from 25% to 35% demonstrated that the Au nanoparticles would shift from clustering within the center of the droplet to the interfacial boundary of the two polymers (as shown in Figure 1-3). While the nanoparticles studied within these aforementioned works were effectively stabilized using the miniemulsion ex situ synthesis technique, substantial nanoparticle aggregates (on the order of 100 nm) were still observed within the polymer droplets for these materials.

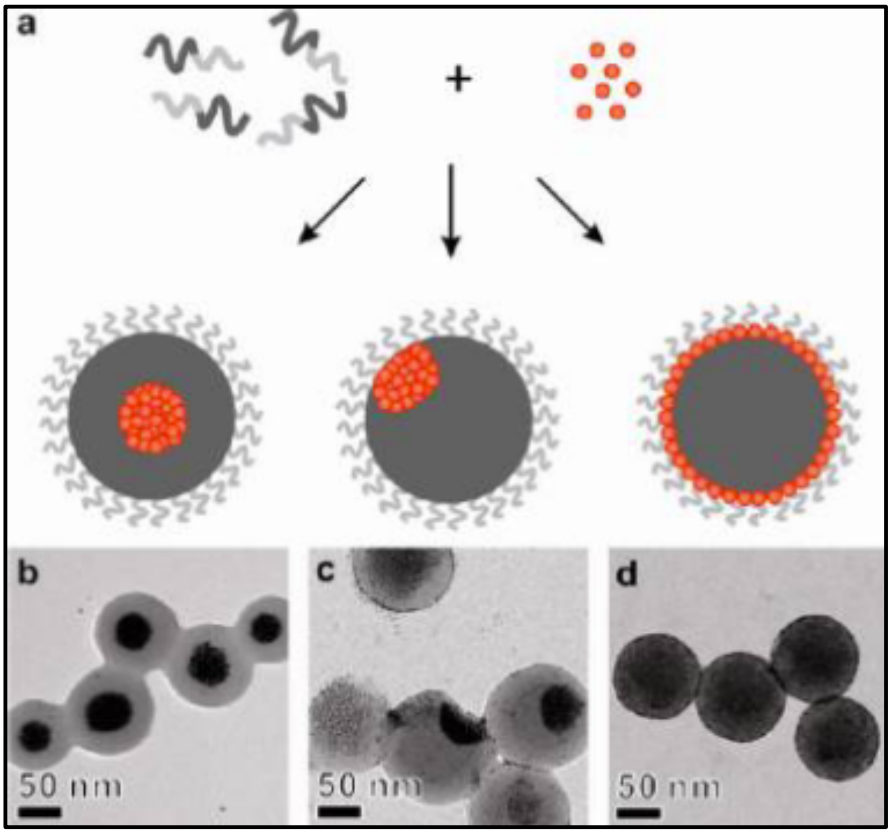

Figure 1-3: **(a)** Schematic of Au nanoparticles being incorporated within polystyrene and polyacrylic co-polymer droplets with varying surface ligands. **(b)** Au nanoparticles clustering in the center of co-polymer droplets using 100% DT. **(c)** Au nanoparticles clustering near co-polymer droplet surfaces using 75% DT and 25% MUL. **(d)** Au nanoparticles adhered to the surface of co-polymer droplets using 20% DT and 80% MUL. Reprinted with permission from Luo, Q., Hickey, R. J. & Park, S. Controlling the Location of Nanoparticles in Colloidal Assemblies of Amphiphilic Polymers by Tuning Nanoparticle Surface Chemistry. ACS Macro Lett. 2013, 2, 107−111. Copyright © 2013 American Chemical Society.[13]

The issue of nanoparticle agglomeration can be more effectively circumvented by using in situ nanoparticle generation techniques. This approach enables the formation of extremely small nanoclusters (with diameters on the order of 10 nm) that can be dispersed in a well-ordered manner. For example, Guo et al. have reported that TiO_2 nanoparticles can be incorporated into a polymer matrix using conventional sol-gel chemistry methods.[14] In their work, titanium (IV) isopropoxide (TTIP) was hydrolyzed using a mixture of ethanol and HCl to yield TiO_2 nanoparticles. The TiO_2 sol was subsequently mixed with monomers and photoinitiators that enabled the encapsulation of 5 nm TiO_2 particles within a polymer matrix. Similarly, Bao et al. have optimized the chemical reagent concentrations for fabricating relatively monodisperse Au nanoparticles (2.7 ± 0.5 nm in diameter) within poly(amidoamine) dendrimers with surface hydroxyl groups.[15]

The synthesis of polymer nanocomposite materials has also been achieved with in situ techniques that confine inorganic nanoparticle crystallization using polymer micelles or vesicles. With this approach, Xu et al. have demonstrated that wet-chemistry methods can be used to form Cu_2O/polyethylene glycol (PEG) composite nanospheres.[16] The adsorption of additional aggregated PEG micelles onto the surface of these composite nanospheres creates mesopores, ultimately controlling the inter-particle spacing of the polymer nanocomposite material. Further experiments conducted by Zhang et al. have demonstrated that the outer surface of polymer micelles can be used as nucleation sites for Ag or Au metal nanoparticles.[17] Upon mixing polystyrene (PS) with an appropriate metal salt precursor in a solvent mixture of acetone and ethanol, metal nanoparticle growth can be controlled on the surface of

PS micelles (as shown in Figure 1-4).

Metal nanoclusters have also been encapsulated within polymer matrices using layer-by-layer (LbL) polyelectrolyte (PE) deposition methods. Wang et al. have combined the LbL technique with an in situ sol-gel process to fabricate metallic core-shell and hollow nanostructures.[18] By incorporating lithium niobate or TiO_2 metal precursors into an alcohol solution containing PE-coated colloids formed using LbL deposition, hydrolysis can occur and condensation of the metal precursors infiltrates the PE layers. Other in situ techniques have relied on the use of diblock copolymers for controlling the morphology and size distribution of metallic nanoparticles. Taubert et al. have reported that a water-soluble poly(ethylene oxide-block-methacrylic acid) (P(EO-b-MAA)) diblock copolymer can be used to modify the size

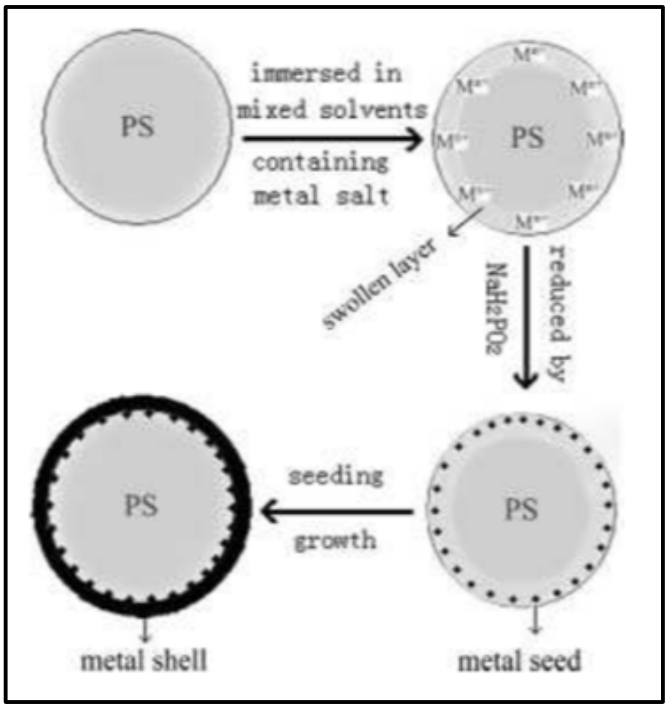

Figure 1-4: Schematic illustration of seeding procedure for coating polystyrene (PS) colloids with metallic nanoparticles. Reprinted with permission from Zhang, B. J. et al. Facile Methods to Coat Polystyrene and Silica Colloids with Metal. 1089–1096 (2004). Copyright © 2004 WILEY-VCH Verlag.[17]

distribution of zinc oxide nanoparticles by changing each block's degree of polymerization.[19]

The results reported above highlight the scientific community's efforts to advance and optimize general synthesis techniques for developing polymer nanocomposites. These contributions have paved the path forward for designing novel materials needed to advance existing technologies. The utility and direct application of these hybrid composite structures span across multiple engineering disciplines.

1.3 Potential Applications

The incorporation of nanostructures into polymers has facilitated the development of new transparent materials that are well-suited for photovoltaic solar cells. Within the Rayleigh light scattering regime, nanoparticles with diameters smaller than the wavelength of light will exhibit scattering efficiencies (Q_{sca}) governed by the following equation:

$$Q_{sca} = \frac{8}{3} \cdot \left(\frac{2\pi n_m a}{\lambda}\right)^4 \cdot \frac{(n_p/n_m)^2 - 1}{(n_p/n_m)^2 + 2}$$

where a is the diameter of the nanoparticle, λ is the wavelength of incident light on the nanoparticle, and n_p and n_m are the refractive indices of the nanoparticle and the surrounding polymer matrix, respectively. Hence, the scattering efficiency of a polymer nanocomposite material can be modified by varying the size of the encapsulated nanoparticles and the refractive indices of the nanoparticles and polymer matrix. Recently, Imai et al. have demonstrated that the total scattering loss can be

diminished by incorporating TiO_2 and ZrO_2 nanoparticles into a poly(bisphenol A carbonate) (PC) matrix (as shown in Figure 1-5).[20] Similarly, Guan et al. have optimized a redispersion-polymerization method to synthesize polymer nanocomposites that exhibit high transmission coefficients for visible light.[21] Ongoing efforts to enhance the mechanical and thermal stability of these transparent materials could contribute to new solar cell designs for advancing renewable energy technologies.[22]

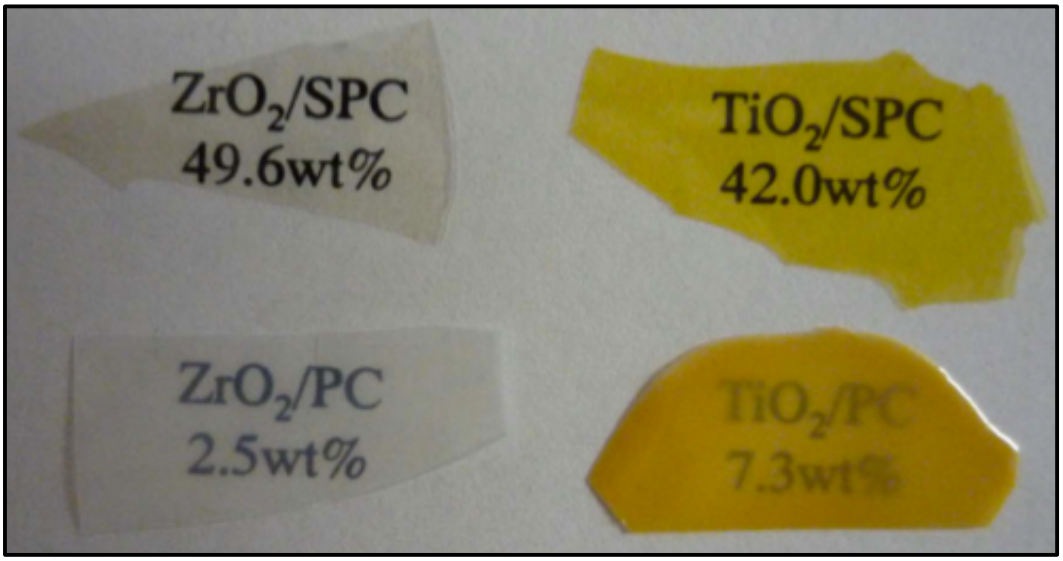

Figure 1-5: Photograph demonstrating the varying optical properties of polymer nanocomposite materials comprised of TiO_2 or ZrO_2 nanoparticles embedded within poly(bisphenol A carbonate) (PC) and sulfonic-acid modified PC (SPC) matrices. Reprinted from Imai, Y. et al. Transparent poly(bisphenol A carbonate)-based nanocomposites with high refractive index nanoparticles. Eur. Polym. J. 45, 630–638, Copyright © 2009 with permission from Elsevier.[20]

As illustrated in Figure 1-6, the magnetic properties of nanoparticles will vary with size.[23–25] Upon encapsulating these nanostructures within a polymer matrix, the resulting composite material may exhibit no magnetic hysteresis. Schmidt has reported that ring-opening polymerization processes can be used to encase Fe_3O_4 nanoparticles to synthesize ferrofluids with superparamagnetic behavior.[26] Yang et al. have demonstrated that polyaniline/Fe_3O_4 microsphere composites can be prepared with useful electromagnetic properties to function as microwave absorbing materials.[27] These novel polymer nanocomposite materials could lead to the development of improved magnetic resonance imaging (MRI) contrast agents and drug carriers for biomedical applications.[28,29]

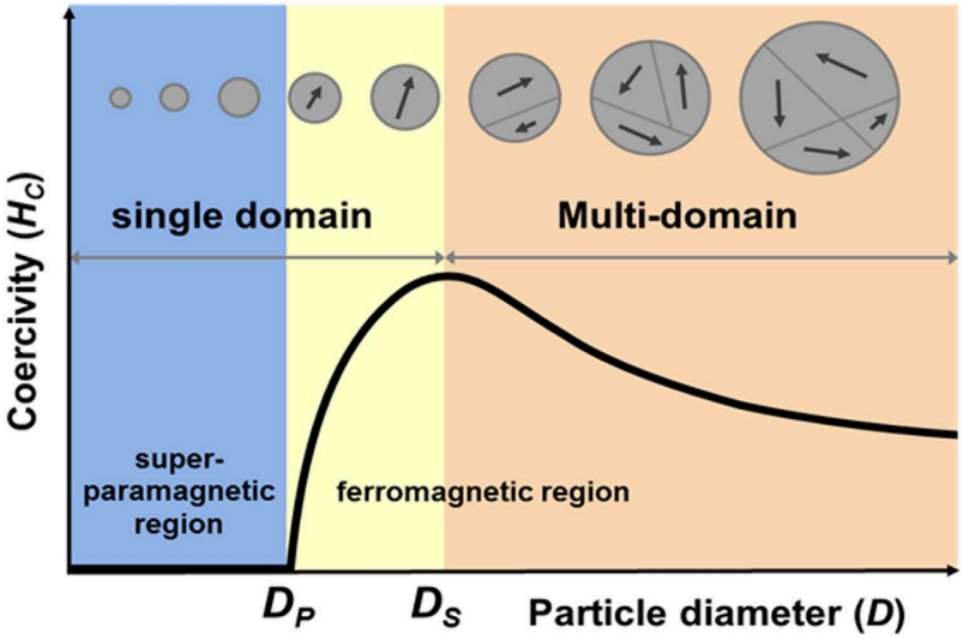

Figure 1-6: Illustrative plot of magnetic coercivity versus nanoparticle diameter. Reprinted from Lee, J. S., Myung Cha, J., Young Yoon, H., Lee, J.-K. & Kim, Y. K. Magnetic multi-granule nanoclusters: A model system that exhibits universal size effect of magnetic coercivity. *Sci. Rep.* **5,** 12135 (2015). Available from: http://dx.doi.org/10.1038/srep12135. This material was originally published by Nature Publishing Group as an open access work and has been reprinted in accordance with the CC BY 4.0 license. Full terms found at https://creativecommons.org/licenses/by/4.0/legalcode.[25]

The utility of embedding nanoparticles into polymers has also extended into the field of microelectronics. For example, the miniaturization of capacitors requires thin materials (no thicker than 100 micrometers) to exhibit high electrical permittivity values.[30] The dielectric constant of a polymer system can be raised using ceramic nanoparticles. The electrical permittivity of perovskite ceramic particles has been observed to vary with size at the nanoscale.[31,32] Multiple research groups have reported increases in the dielectric constant of a polymer nanocomposite system by incorporating high k-value $BaTiO_3$ nanoparticles into polymer matrices.[33–35] The development of these hybrid materials are expected to facilitate the fabrication of more powerful capacitors, resistors, and transistors, yielding a new generation of microelectronic devices for printed circuit boards.

As mentioned previously, polymer nanocomposites have also supported the development of improved battery electrodes. Within Li-ion batteries, incorporating nanoparticles within electrode materials can enhance lithium insertion and removal by decreasing the characteristic time constant for diffusion.[36] Using micro-emulsion techniques, Wang et al. have synthesized composite materials using Sn-based nanoparticles within a graphite framework.[37] The incorporation of Sn or SnO_2 nanoparticles have improved battery cycling and mitigated electrode pulverization. Yao et al. have taken this research a step further by designing Sn-graphene nanocomposites.[38] Alternatively, Xiao et al. have studied the battery cycling stability improvements associated with incorporating MoS_2 nanoparticles into a polyethylene oxide (PEO) matrix.[39] Novel polymer-based electrolyte materials incorporating Li salt

and Al_2O_4 nanoparticles into a PEO matrix have also been synthesized and reported to increase the interfacial stability between the electrodes and the electrolyte.[40,41]

The findings presented above underscore the broad application of polymer nanocomposite materials for emerging biomedical, electrical, magnetic, and optical technologies. Understanding the primary mechanisms that underlie the formation of these polymer nanocomposite materials will be indispensable for designing innovative synthesis methods that allow one to control the morphology and dispersion of nanostructures within polymers. Such efforts will support ongoing research initiatives to develop advanced materials that exploit the unique properties of inorganic-organic composite structures.

1.4 Scope of Study

Herein, I investigate the underlying processes that drive metallic nanoparticle formation and growth within a polymer matrix. I employ a conventional aerosol spray pyrolysis (ASP) technique that uses a pneumatic atomizer to synthesize polymer nanocomposite materials. This in situ synthesis method nebulizes an aqueous solution containing a metal salt precursor and a water-soluble polymer to generate an aerosol. The produced aerosol can subsequently be passed through a reactor to thermally decompose the metal salt into the desired product. Incorporating a polymer into the ASP precursor solution has been reported to drastically modify the structure/ordering, morphology, and size distribution of the metallic nanoparticles generated using this technique.

Brinker et al. have reported the development of an ASP synthesis method that incorporates organic monomers and thermal initiators into the precursor solution to

control the mesostructure of silica-polymer nanocomposites.[42] By varying the molar concentration of the organic components within the precursor solution, silica polymer nanocomposites can be synthesized with either "puckered vesicular" or "reticulated foam" mesostructures (as shown in Figure 1-7).[42] Similarly, Tsung et al. have incorporated amphiphilic copolymers into ASP precursor solutions to synthesize mesoporous metal oxide materials.[43] By dissolving metal alkoxides into a mixture of acetic acid, hydrochloric acid, and ethanol (AcHE), the precursor particles are organized into a copolymer framework and exhibit nano-crystalline domains (as shown in Figure 1-8). In a different manner, Suh et al. synthesized porous nanospheres by incorporating organic monomers with a radical initiator into a

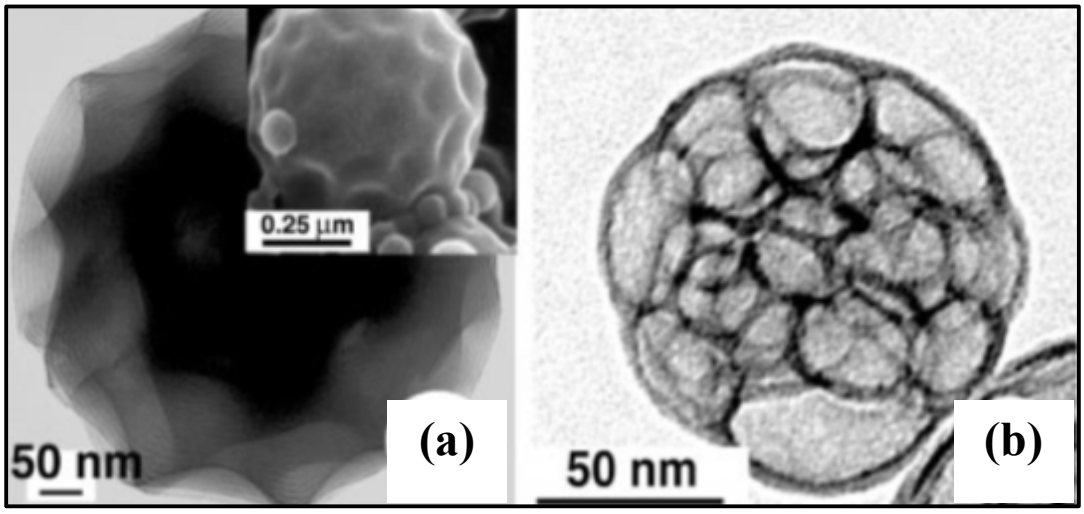

Figure 1-7: TEM micrographs of a silica/polymer nanocomposite particle showing a **(a)** "puckered vesicular" microstructure and **(b)** a "reticulated foam" structure prepared using different concentrations of organic components within the ASP precursor solution. Adapted with permission from Macmillan Publishers Ltd: Nature (Brinker, C. J. et al. Aerosol-assisted self-assembly of mesostructured spherical nanoparticles. Nature, 398, 223–226), Copyright © 1999.[42]

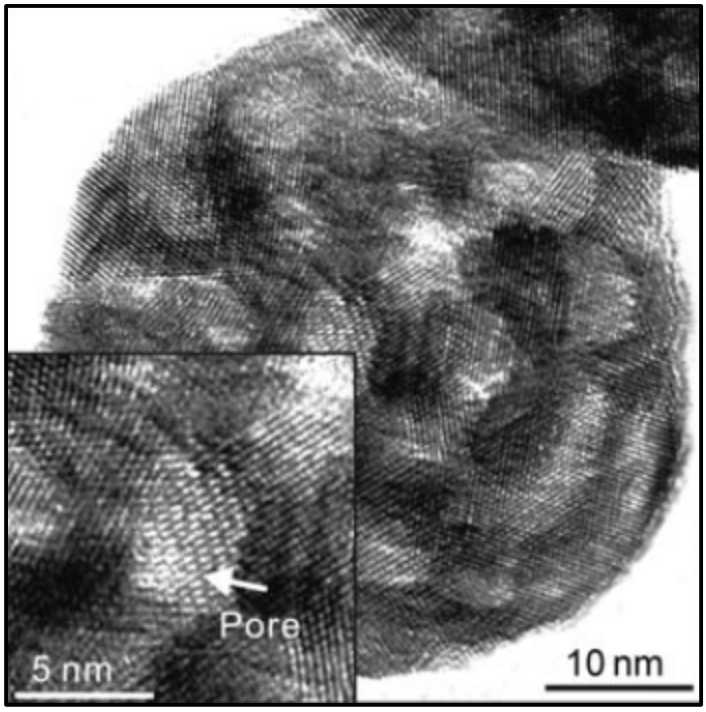

Figure 1-8: HRTEM image of a mesoporous ZrO_2 sphere prepared using ASP exhibiting nano-crystalline domains. Adapted with permission from Tsung, C. K. et al. A general route to diverse mesoporous metal oxide submicrospheres with highly crystalline frameworks. Angew. Chemie - Int. Ed. 47, 8682–8686 (2008). [43]

colloidal solution of silica nanoparticles.[44] By generating an aerosol that initially passes through a low temperature furnace (200˚C) and then a high temperature furnace (700˚C), silica nanoparticles (approximately 12 nm in diameter) were strategically guided into spherical agglomerates during the polymerization reaction in the first furnace and then made mesoporous upon thermally decomposing the polymer in the second furnace.

In addition to modifying the structure and dispersion of nanoparticles generated using ASP, polymers have also been used to manipulate their morphology and arrest their growth. For example, Kang et al. have demonstrated that ZrO_2 hollow

nanostructures originally synthesized from an aqueous solution can be solidified (filled-in) by incorporating a polymer into the ASP precursor solution.[45] Similar effects have been reported for ceria nanoparticles synthesized using ASP.[46] To achieve a narrower size distribution for $LiNi_{0.8}Co_{0.15}Mn_{0.05}O_2$ nanoparticles, Ju et al. have used critic acid and ethylene glycol as polymeric precursors within their ASP experiments.[47] Moreover, Kim et al. have reported that the size distribution of Ag nanoparticles embedded in polyvinylpyrrolidone (PVP) or polyvinyl alcohol (PVA) can be controlled by varying the concentration and molecular weight distribution of polymer within a $AgNO_3$ ASP precursor solution.[48] Further research by Lee et al. has proposed that a decrease in the size distribution of Ag nanoparticles encapsulated in PVP is correlated with an increase in molecular weight due to higher mobility and enhanced coagulation of lower molecular weight PVP chains.[49]

My research, presented hereafter, is intended to support the scientific community's ongoing efforts to understand how polymers can be used to manipulate the physical characteristics of metallic nanostructures. Specifically, my work analyzes the growth and stabilization of Ag and Ni nanoclusters generated using ASP. These nanoclusters were synthesized using precursor solutions that incorporated different water-soluble polymers such as polyvinylpyrrolidone (PVP), polyethylene glycol (PEG), and polyethylene oxide (PEO). By varying different experimental process variables such as the polymer system's molecular weight, the metal salt to polymer mass ratio within the ASP precursor solution, and the temperature of the tube furnace reactor, I have identified important parameters that govern nanocluster formation. Having analyzed the correlations that exist between these parameters and the physical

properties of the polymer nanocomposite systems synthesized, I propose a qualitative model for understanding the growth mechanisms that control the formation of monodisperse metallic nanoclusters within a polymer matrix using ASP.

Chapter 2: Synthesis of Ag and Ni Polymer Nanocomposites

2.1 Aerosol Spray Pyrolysis

Aerosol spray pyrolysis (ASP) is a synthesis method for generating nanoparticles. Using this technique, a precursor solution can be nebulized to produce an aerosol that can be passed through a reactor to expedite solvent evaporation and thermally decompose a metal salt precursor. I chose to synthesize Ag and Ni nanostructures to demonstrate that this particular synthesis technique can be used to generate various types of metallic nanoclusters that exhibit different kinds of interesting properties. Ag nanoparticles, for example, have antimicrobial properties that make them well-suited for emerging biomedical technologies.[50] Alternatively, Ni nanoparticles exhibit superparamagnetic behavior that could be used to develop ferrofluids for designing effective dynamic seals or heat dissipation systems.[51,52] The adaptability and scalability of this particular technique potentially lends itself to synthesizing different types of polymer nanocomposite materials using different types of metals.

Figure 2-1 shows a schematic of my experimental apparatus for synthesizing polymer nanocomposite materials using ASP. A conventional ASP set-up consists of three primary components: (i) an atomizer, (ii) a tube furnace reactor, and (iii) a particle collector. Atomizers used to nebulize the precursor solution can be pneumatic, ultrasonic, or electrostatic. Pneumatic nozzles produce an aerosol using a pressurized gas. Ultrasonic nozzles generate high frequency sound waves on a liquid surface to atomize the solution. Electrostatic nozzles rely on exposing a charged liquid to an electric field to disperse the liquid into fine particles through a process

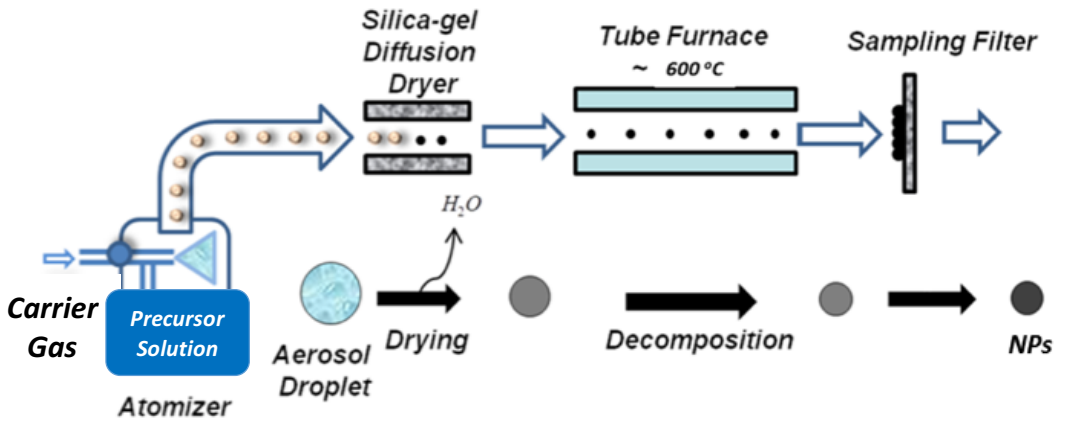

Figure 2-1: Schematic illustration of the aerosol spray pyrolysis apparatus used to generate polymer nanocomposite materials.

in which coulombic repulsion overcomes surface tension of the emitted droplets.[53] If the solvent used for the precursor solution is water, an intermediary silica-gel diffusion dryer can be introduced before the aerosol reaches the tube furnace. This additional component facilitates solvent evaporation. After atomization, pyrolysis of the metal precursor takes place within the tube furnace reactor. The nature of the metal precursor decomposition can depend on the concentration of the metal precursor solution, the carrier gas, the tube furnace temperature, and the carrier gas flow rate. Changes to these experimental parameters have been extensively studied to tune the size distribution and morphology of the collected nanoparticles.[54,55] My experiments used a pneumatic BGI 3-jet collision nebulizer with a liquid feed rate of 4.5 mL/hr to generate droplets with a mass median diameter (MMD) of 2 μm. My apparatus also included a silica-gel diffusion dryer, a quartz tube 0.28 m in length (with a wall thickness of .0031 m and outer diameter of .0254 m) introduced within a Lindberg/Blue M Tube Furnace (Model Number: TF55030A-1), and a Millipore Corp. Sample Collector (Catalog Number: XX4404700) equipped with 0.4 μm (pore size) HTTP Isopore^{TM} membrane filter paper.

2.2 Precursor Solution Preparation

The precursor solutions used within my ASP experiments were aqueous solutions comprised of water-soluble metal salts and polymers. The metal salt precursors used to obtain Ag and Ni nanoparticles were $AgNO_3$ and $NiNO_3 \cdot 6H_2O$, respectively. The water-soluble polymers incorporated into the ASP precursor solutions were polyvinylpyrrolidone (PVP), polyethylene glycol (PEG), and polyethylene oxide (PEO). The molar concentration of each of these polymers within the ASP precursor solution was maintained at approximately 10^{-3} to 10^{-5} M. The molar concentration of the $AgNO_3$ and $NiNO_3 \cdot 6H_2O$ metal salt precursor was varied between 10^{-1} to 10^{-3} M and 10^{-2} to 10^{-3} M, respectively, to prepare precursor solutions with different metal salt precursor to polymer mass ratios. A Scientific Industries, Inc. Vortex Genie^{TM} Mixer (Serial No. G8804) was used to facilitate the mixing of the metal salt precursor and polymer components within deionized water to ensure the components had fully dissolved. My ASP experiments would typically use a carrier gas flow rate of 3LPM and a 15 mL precursor solution, taking approximately three hours to complete.

2.3 Process Variables

Within my ASP experiments, the following process variables were investigated: the mass ratio of metal salt to polymer within the precursor solution, the tube furnace reactor temperature, the carrier gas flow rate, and the polymer system's molecular weight. By varying the mass ratio of the metal salt and polymer components within the precursor solution, I evaluated whether using lower concentrations of the metal salt precursor would yield smaller metallic nanoparticles

within the polymer matrix. Upon varying the mass ratio of PVP to $AgNO_3$ within ASP precursor solutions, Lee et al. have observed that the resulting Ag crystallite diameter can be substantially lowered from 30 nm to 5 nm by increasing the concentration of PVP.[49] I also varied the tube furnace reactor temperature to find the optimal temperature for decomposing the metal salt precursor and generating extremely small nanoclusters within the polymer. To modify the residence time of the aerosol within the tube furnace, the carrier gas flow rate was varied. This process variable was studied to determine if the metal salt precursor could be fully decomposed using a strategic combination of higher temperatures and shorter residence times. Lastly, the molecular weight of the polymer system was varied to determine if the length of the polymer chains affected the growth of metallic nanoparticles within the polymer matrix. Lee et al. have reported that increasing the molecular weight of PVP within the precursor solution from 10,000 to 30,000 reduces the diameter of Ag nanoparticles from 10 nm to 6 nm.[49] These process variables were studied to investigate which type of mechanisms control the formation of polymer nanocomposite materials using ASP.

2.4 Particle Collection

Within a conventional ASP apparatus, the synthesized particles are collected using a filtration mechanism. By passing the aerosol through a piece of filter paper comprised of a mat of fine fibers oriented perpendicular to the flow of the carrier gas, particles can be collected by means of impaction, interception, or diffusion.[56,57] In my ASP experiments, I also collected particles using a cold finger inserted within the

tube furnace reactor (as illustrated in Figure 2-2). This cold finger was comprised of an aluminum foil substrate adhered to the surface of copper tubing connected to a water cooling pump. By maintaining the aluminum substrate at a colder temperature than that of the tube furnace, I sought to collect particles via thermophoresis. In this manner, I hoped to arrest nanoparticle growth by reducing the residence time of the aerosol and quenching the polymer nanocomposite system.

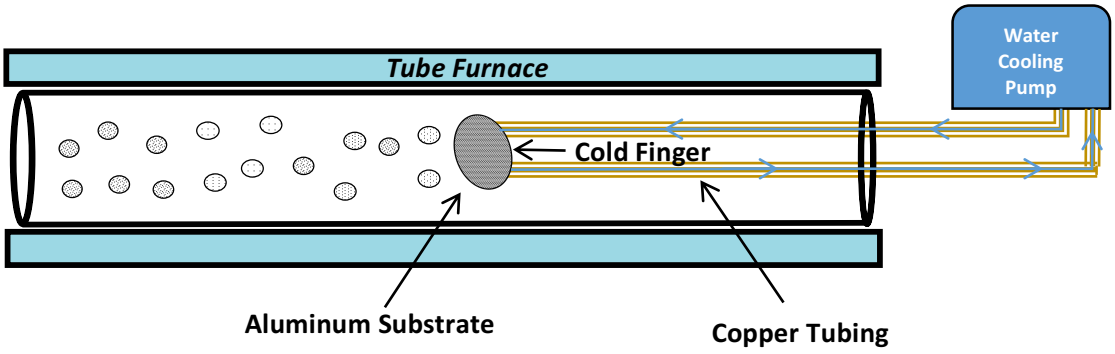

Figure 2-2: Schematic illustration of a cold finger used to collect nanoparticles on an aluminum substrate via thermophoresis.

Chapter 3: Materials Characterization Methods

3.1 X-ray Diffraction (XRD)

X-ray diffraction (XRD) was used to confirm that the $AgNO_3$ and $NiNO_3 \cdot 6H_2O$ metal salt precursors had fully decomposed into their respective metals during the aerosol spray pyrolysis (ASP) experiment. My XRD data was collected using a Bruker D8 diffractometer with Cu Kα radiation at the University of Maryland X-ray Crystallographic Center. Thermodynamic data presented in the literature indicates that $AgNO_3$ will fully decompose into pure elemental Ag around 440˚C.[58] Since the particles produced by the pneumatic atomizer in these experiments have diameters on the order of 10^{-6} meters, I initially assumed that every microscale droplet passed through the 0.28 meter tube furnace reactor would likely be heated to the set furnace temperature. To confirm this for my experimental apparatus, initial ASP experiments were conducted using aqueous precursor solutions that included the metal salt (e.g., $AgNO_3$) without any polymer. Figure 3-1 shows the different XRD patterns for nanoparticles synthesized from a $AgNO_3$ precursor solution passed through a tube furnace at 500˚C and 600˚C using an argon (Ar) carrier gas. This XRD data demonstrates that elemental Ag can only be obtained by decomposing $AgNO_3$ at a tube furnace temperature of 600˚C. However, the XRD data presented in Figure 3-2 indicates that the introduction of PVP into the precursor solution can notably alter the metal salt decomposition temperature so that the $AgNO_3$ can be fully decomposed into elemental Ag at temperatures as low as 400˚C. This result is in agreement with the findings of Lee et al.[49]

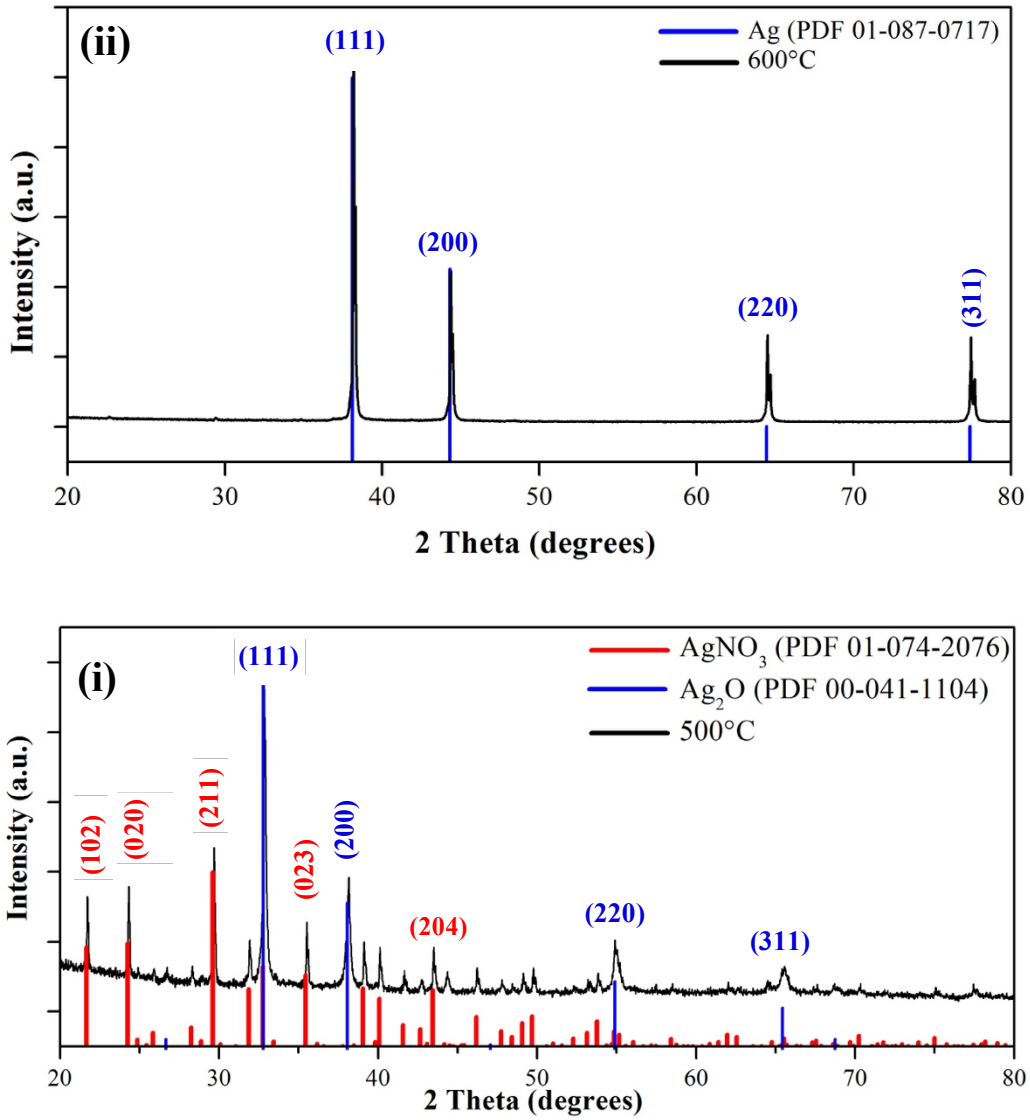

Figure 3-1: XRD data collected for nanoparticles synthesized using an ASP aqueous precursor solution of $AgNO_3$ without any polymer at **(i)** 500˚ C and **(ii)** 600˚C. The peaks labeled for the 600°C sample confirm that the $AgNO_3$ has decomposed to Ag.

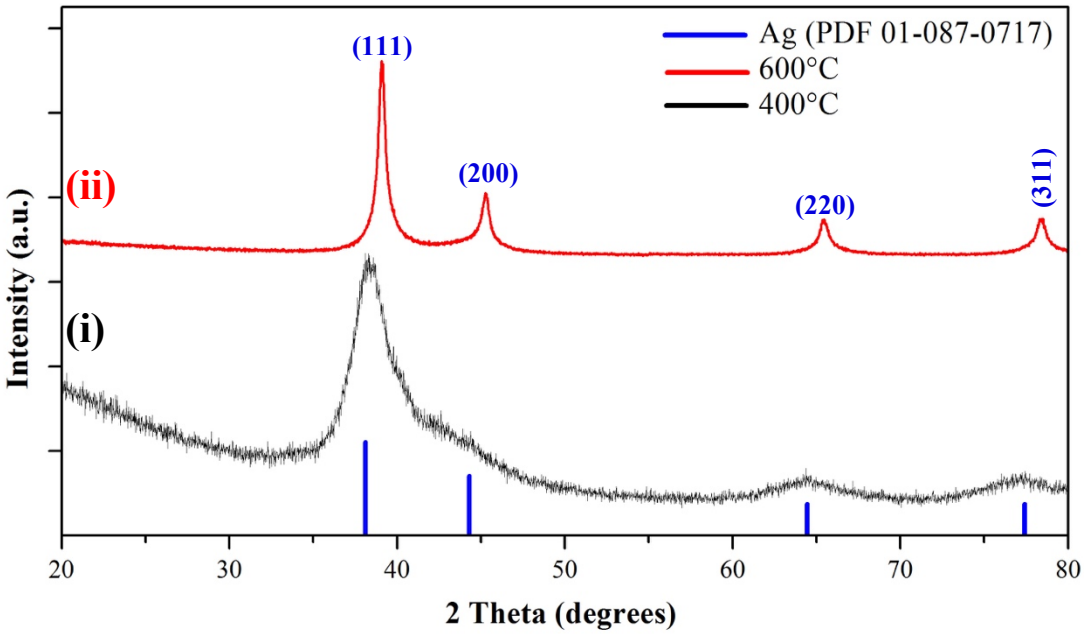

Figure 3-2: XRD data collected for nanoparticles synthesized using an ASP aqueous precursor solution of $AgNO_3$ and PVP at **(i)** 400˚ C and **(ii)** 600˚C. The peaks labeled confirm that $AgNO_3$ has been decomposed to Ag using both temperatures.

Similarly, a $NiNO_3 \cdot 6H_2O$ precursor solution was atomized and passed through a tube furnace at different temperatures with a gas mixture of 5% H_2 and 95% N_2. $NiNO_3 \cdot 6H_2O$ has been reported to decompose into NiO at 573˚C and be further reduced to elemental Ni at 535˚C with a 10% H_2 and 90% N_2 gas mixture.[59] Figure 3-3 shows XRD data for nanoparticles synthesized from a $NiNO_3 \cdot 6H_2O$ metal salt precursor solution without the introduction of any polymer. This XRD data confirms that $NiNO_3 \cdot 6H_2O$ can only be fully decomposed and reduced to Ni at temperatures of 600˚C and higher. Figure 3-4 demonstrates that elemental Ni can also be obtained at 600˚C with the introduction of PVP, PEG, or PEO polymers into the precursor solution by means of pyrolysis and hydrogen reduction.

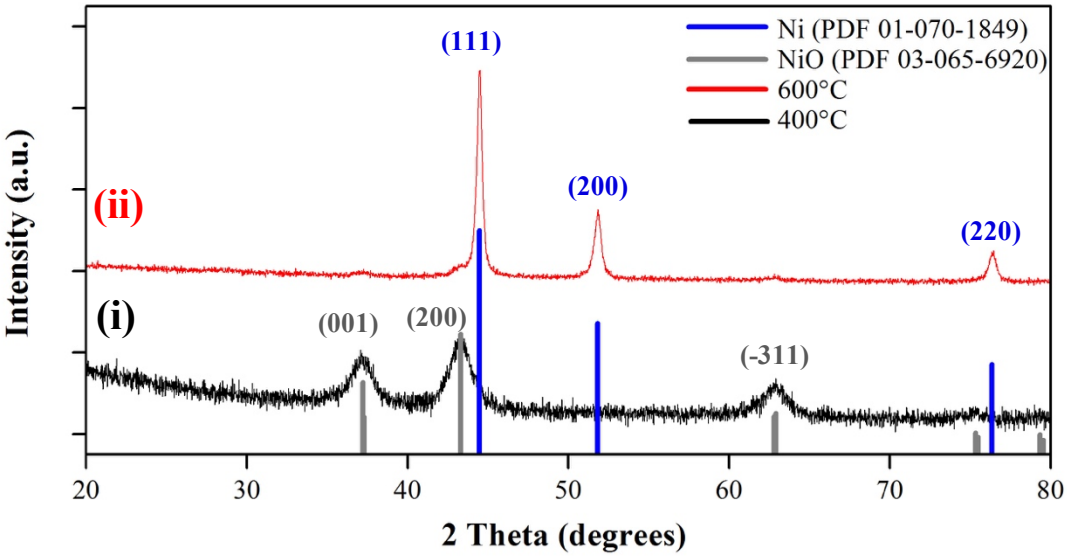

Figure 3-3: XRD data collected for nanoparticles synthesized using an ASP aqueous precursor solution of $NiNO_3 \cdot 6H_2O$ without any polymer at **(i)** 400˚ C and **(ii)** 600˚C. The peaks labeled in (ii) demonstrate that $NiNO_3 \cdot 6H_2O$ can be decomposed and reduced to Ni at 600˚C.

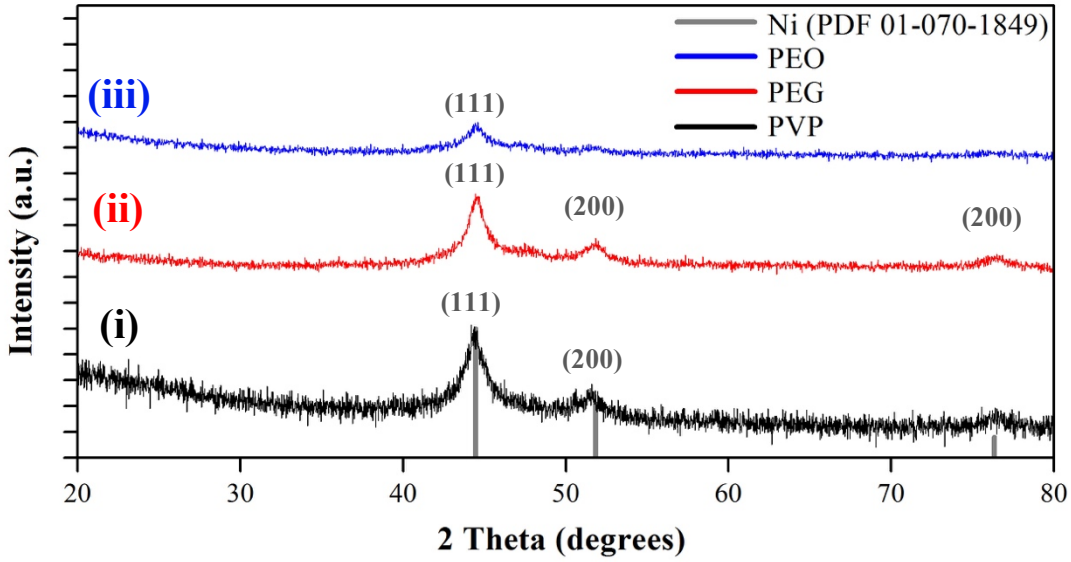

Figure 3-4: XRD data collected for nanoparticles synthesized using an ASP aqueous precursor solution of $NiNO_3 \cdot 6H_2O$ with **(i)** PVP, **(ii)** PEG, or **(iii)** PEO at 600˚C. The labeled peaks demonstrate that $NiNO_3 \cdot 6H_2O$ can be decomposed and reduced to Ni when a polymer is incorporated into the precursor solution.

The diffraction patterns presented above were further analyzed using Le Bail refinement with TOPAS 4.2 software.[60] This technique uses predetermined unit cell parameters and crystal space group classifications from powder diffraction files (PDFs) to extract peak intensities from the collected diffraction data. The fitting algorithm employed in this analysis refines the unit cell parameters to generate a curve that matches the measured XRD pattern. Subsequently, the full width at half maxima (FWHM) of each Bragg peak was measured and used in the Scherrer equation to estimate the diameter of the crystallite domains within the metallic nanostructures.[61] The results of this analysis, presented in Table 3-1, demonstrate that the incorporation of a water-soluble polymer into the metal salt precursor solution can yield metallic nanoclusters with crystalline domains exhibiting diameters of less than 20 nm.

Polymer Nanocomposite System	Furnace Temperature (˚C)	Space Group	Crystallite Size (nm)
Ag-PVP	400	Cubic (Fm-3m)	**2.8**
Ag-PVP	600	Cubic (Fm-3m)	**11.3**
Ni-PVP	600	Cubic (Fm-3m)	**3.7**
Ni-PEG	600	Cubic (Fm-3m)	**5.4**
Ni-PEO	600	Cubic (Fm-3m)	**2.9**

Table 3-1: Crystallite domain size of metallic nanoclusters within different polymer nanocomposite systems estimated using Le Bail refinement and the Scherrer equation from acquired XRD data.

3.2 Fourier Transform Infrared Spectroscopy (FTIR)

Fourier transform infrared spectroscopy (FTIR) was used to analyze the structure of the polymer coating on the collected metal nanoparticles and evaluate if any substantial polymer degradation had taken place within tube furnace reactor. Figure 3-5 shows the absorbance spectrums for pure PVP and for a Ag-PVP polymer nanocomposite sample synthesized using ASP. Both spectrums have characteristic peaks at the same wave numbers and demonstrate that the PVP did not fully decompose in the tube furnace yielding only a carbon coating on the surface of the Ag nanoparticles.

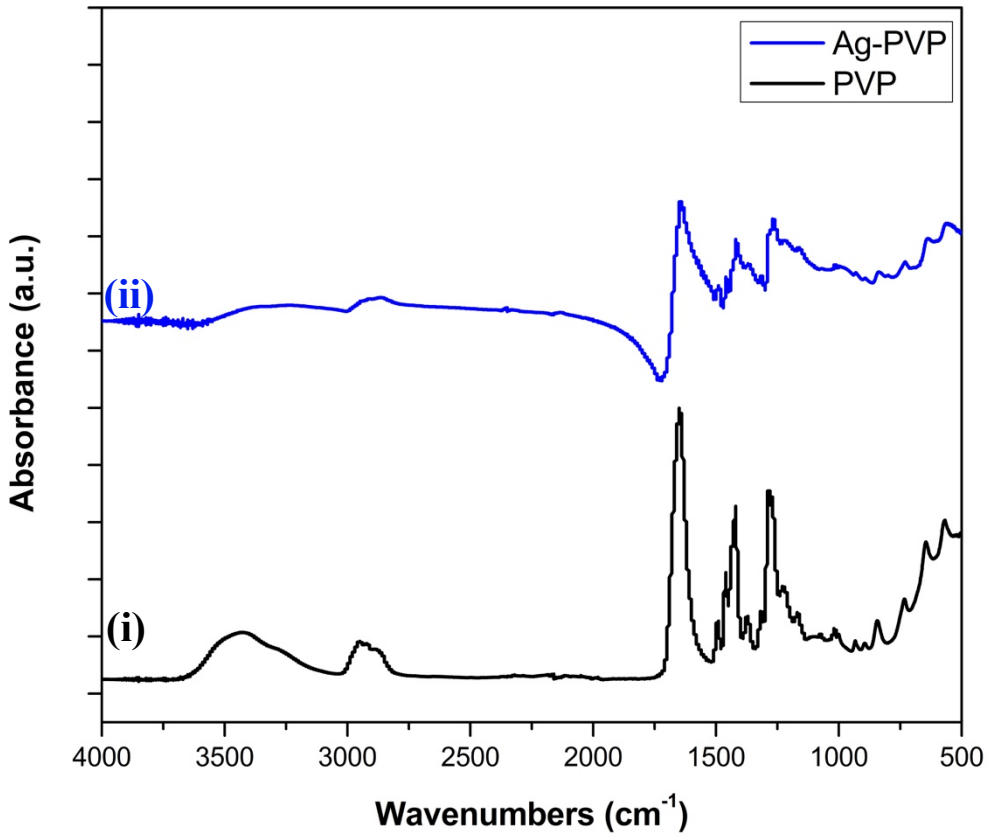

Figure 3-5: FTIR data collected for **(i)** pure PVP and **(ii)** a Ag-PVP polymer nanocomposite sample synthesized using ASP. The characteristic peaks observed at the same wavenumbers for each absorbance spectrum demonstrates that the PVP did not thermally decompose within the tube furnace.

3.3 Scanning and Transmission Electron Microscopy (SEM and TEM)

Scanning electron microscopy (SEM) and transmission electron microscopy (TEM) techniques were used to analyze the morphology and size distribution of the polymer nanocomposite samples. A Hitachi SU-70 FEG SEM and a JEOL JEM 2100 LaB_6 TEM made available by the Advanced Imaging & Microcopy Lab (AIMLab) at the Maryland Nanocenter were used to acquire SEM and TEM micrographs. Figure 3-6 (a) is a TEM image of pure Ag particles synthesized using the ASP process. Upon introducing PVP into the metal precursor solution, it is observed that the diameter of the Ag particles synthesized using ASP are substantially reduced as shown in Figure 3-6 (b).

The encapsulation and distribution of these smaller Ag nanoparticles within a polymer matrix is also illustrated in the SEM micrographs presented in Figure 3-7. Figure 3-7 (a) depicts the formation of pure PVP particles without any encapsulated metallic nanoclusters using ASP. Figure 3-7 (b) shows the deposition of metallic nanoclusters within these polymer droplets upon incorporating a metal additive within the ASP precursor solution. This micrograph demonstrates that Ag nanoparticle growth is arrested by the surrounding polymer medium, yielding metallic nanoclusters with spherical morphology and a fairly monodisperse size distribution.

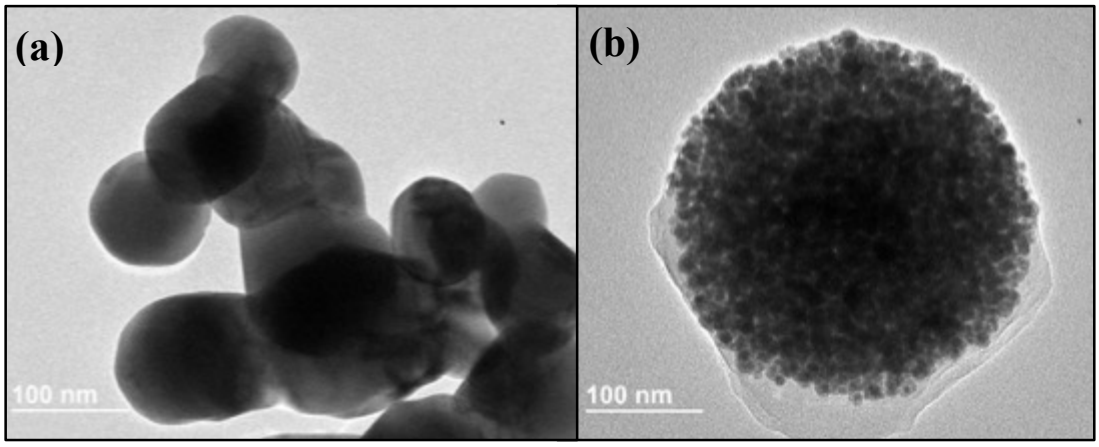

Figure 3-6: TEM micrographs of **(a)** Ag nanoparticles and **(b)** Ag-PVP polymer nanocomposite sample synthesized using ASP. These images demonstrate how the introduction of PVP into the ASP precursor solution can be used to substantially reduce the diameter of the Ag nanoparticles.

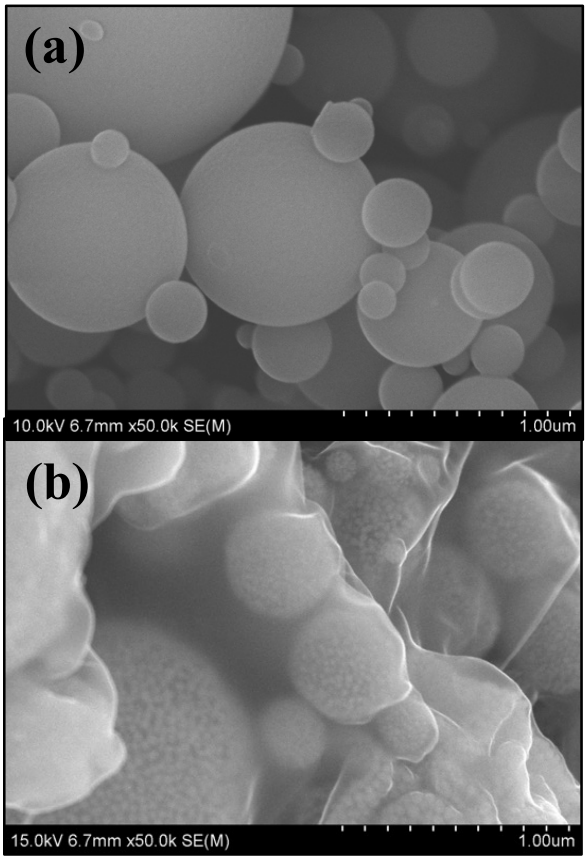

Figure 3-7: SEM micrographs of **(a)** PVP droplets and **(b)** Ag-PVP polymer nanocomposite sample synthesized via ASP. The micrograph presented in **(b)** illustrates the encapsulation and distribution of monodisperse Ag nanoparticles within spherical PVP droplets.

Upon decreasing the metal salt concentration relative to the polymer within the ASP precursor solution, the thickness of the PVP coating surrounding the Ag nanoparticles was observed to increase. This observation is shown in the SEM image presented in Figure 3-8 (a) for a sample synthesized using a $AgNO_3$ to PVP mass ratio of 1 to 10. Upon visual inspection, the Ag nanoparticles are not clearly observed within the spherical PVP droplet. However, energy-dispersive x-ray spectroscopy (EDS) data presented in Figure 3-8 (c) reveals the presence of Ag nanoparticles (shaded in red) beneath the thick layer of PVP.

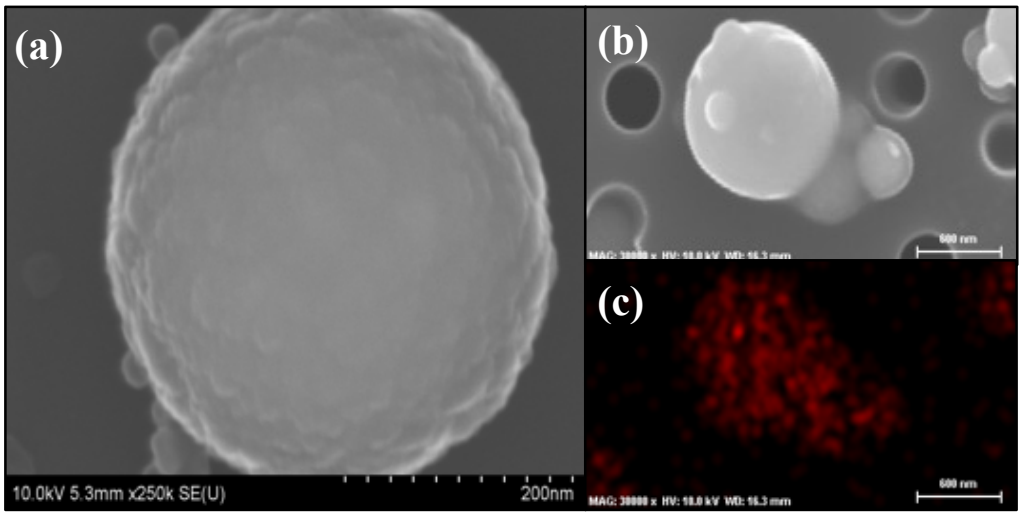

Figure 3-8: (a) and (b) SEM micrographs of Ag-PVP polymer nanocomposite droplets synthesized using a $AgNO_3$ to PVP mass ratio of 1 to 10 within the ASP precursor solution. **(c)** EDS analysis overlaying the micrograph in **(b)** confirming that Ag nanoparticles (shaded in red) are embedded beneath the thick PVP surface.

The PVP matrix effectively immobilizes the Ag nanoparticles until the polymer is dissolved in a solvent such as ethanol, as shown in Figure 3-9. This demonstrates the ability to release and disperse the Ag nanoparticles in a controlled manner suitable for potential biomedical applications. Notably, however, Lee et al. have observed that PVP has a very strong adhesion to the surface of the Ag nanoparticles.[49] Lee et al. demonstrate that after washing the nanoparticles in a solvent such as water, FTIR spectroscopy has shown that a residual layer of PVP is still coated on the surface of the nanoparticles.[49]

As shown in Figure 3-10, this dispersion method also reveals the existence of even smaller nanoparticles previously unobserved in the TEM micrographs. Such an observation demonstrates the limitations of electron microscopy in characterizing the size distribution of these polymer nanocomposites. Polymer nanocomposite samples prepared as thin films for transmission electron microscopy (TEM) must have a remarkably small thickness between 50-70 nm.[62] Otherwise, the electron beam cannot fully survey the nanoparticles embedded deep beneath the outer surface of the polymer coating. To fully investigate the volume fraction of nanoparticles within each polymer droplet, the sample must be cross-sectioned with a microtome before analysis.

Figure 3-11 (a and b) also demonstrates the gradual release of Ag nanoparticles using a high current electron beam to break the covalent bonds of the polymer network. These images, which illustrate the release of the Ag nanoparticles, highlight how the polymer has encapsulated the Ag nanoparticles in a manner that has prevented nanoparticle agglomeration.

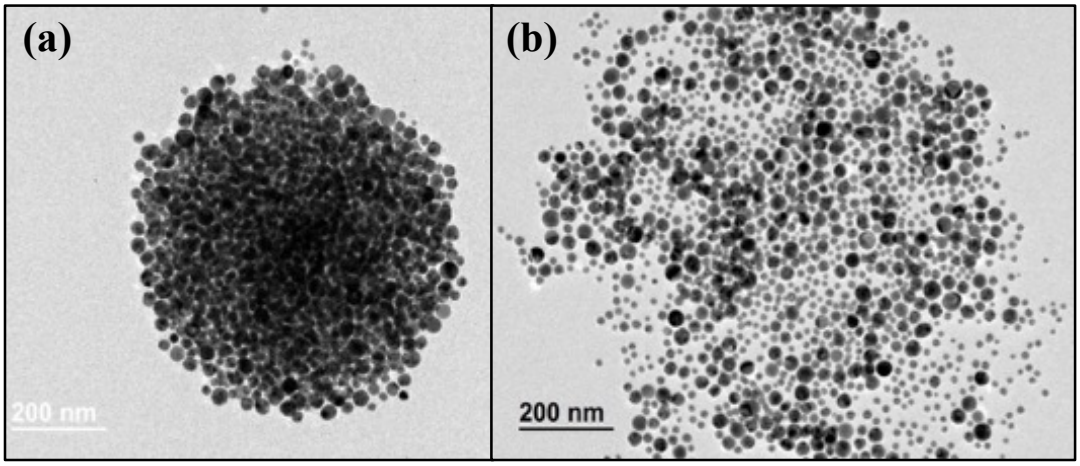

Figure 3-9: TEM micrographs illustrating **(a)** a droplet of Ag nanoparticles immobilized by a PVP matrix and **(b)** the controlled release of Ag nanoparticles from the PVP matrix using ethanol.

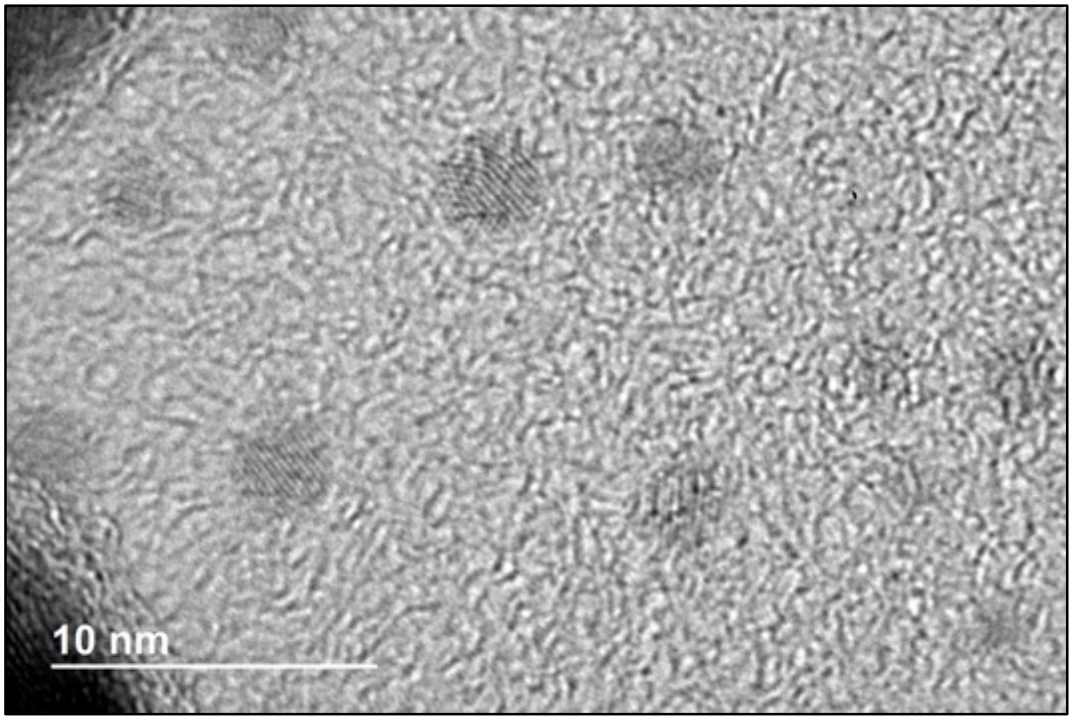

Figure 3-10: TEM micrograph revealing the existence of smaller Ag nanoparticles within the PVP matrix that were unobservable before the Ag nanoparticles were released using ethanol.

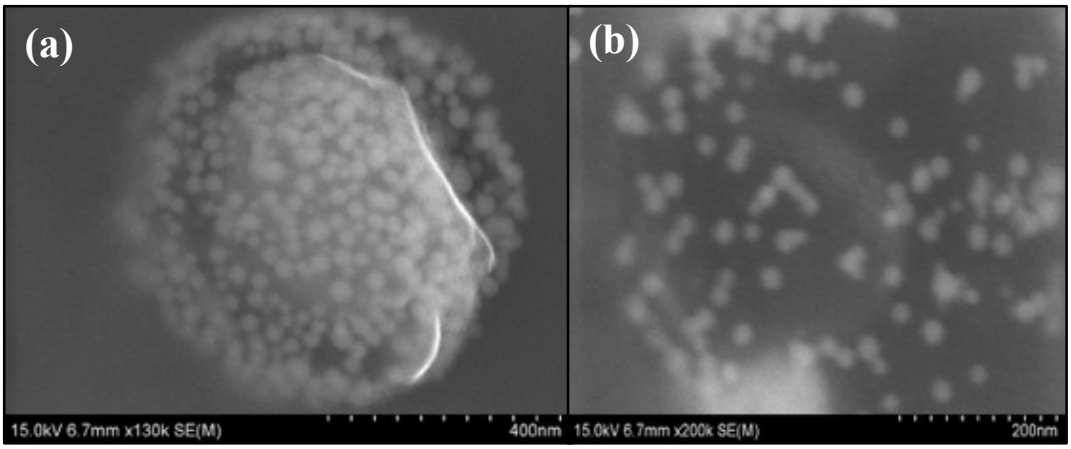

Figure 3-11: SEM micrographs illustrating **(a)** a droplet of Ag nanoparticles immobilized by a PVP matrix and **(b)** the gradual release of Ag nanoparticles from the PVP matrix using a high current electron beam.

Similarly, the diameter of Ni nanoparticles also underwent a substantial size reduction by introducing a polymer into the $NiNO_3 \cdot 6H_2O$ precursor solution. The TEM micrographs presented in Figure 3-12 (a, b, and c) demonstrate the ability of PVP, PEG, and PEO to effectively arrest the growth of Ni nanoparticles. Unlike the spherical PVP droplets containing Ag nanoparticles, however, these polymer droplets containing Ni nanoparticles have a rougher surface texture as shown in the SEM micrographs of Figure 3-13 (a and b). The observed creases formed on the surface of these polymer droplets could be formed from the reduction of NiO with hydrogen. The size of the nanoparticles encapsulated within these polymer droplets would become smaller as this reaction takes place and yields H_2O molecules that would evaporate within the tube furnace. If this reaction were to occur at different rates across the surface of the polymer droplet, then the droplet morphology would become less spherical and even asymmetric as the droplets in Figure 3-13 are observed to be.

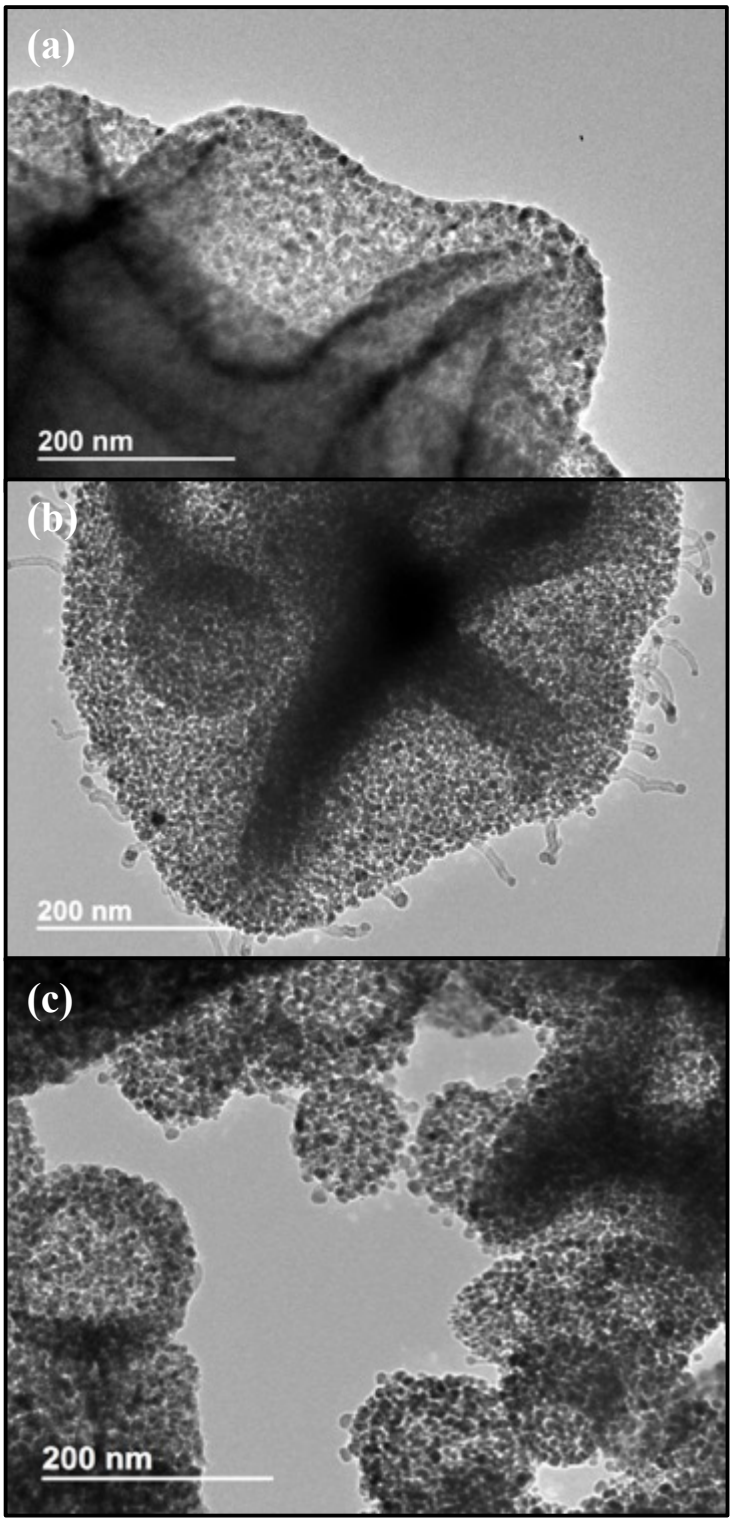

Figure 3-12: TEM micrographs demonstrating the ability to arrest Ni nanoparticle growth by incorporating **(a)** PVP, **(b)** PEG, or **(c)** PEO into a $NiNO_3 \cdot 6H_2O$ ASP precursor solution.

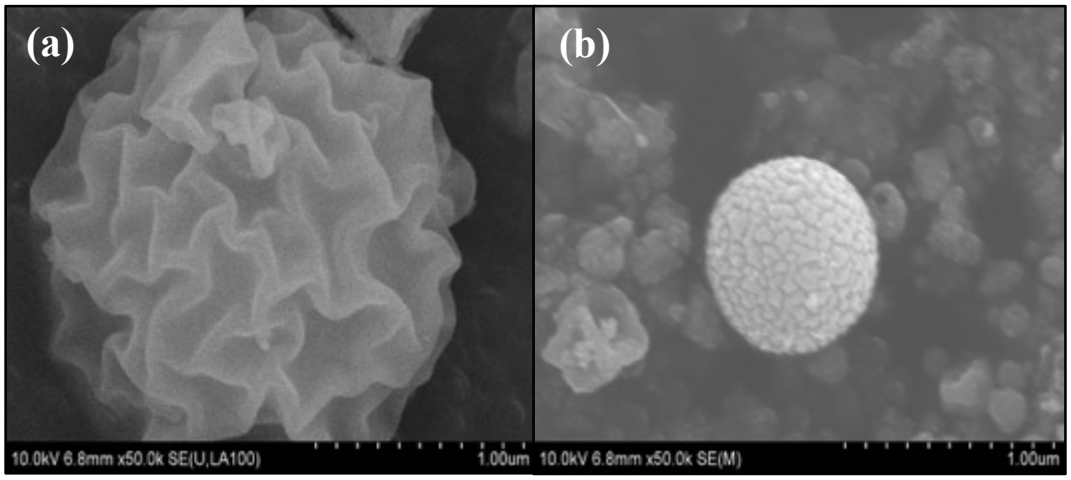

Figure 3-13: SEM micrographs of **(a)** Ni-PVP and **(b)** Ni-PEG polymer nanocomposite droplets observed to have notable surface creases possibly resulting from the reduction of NiO nanoparticles with hydrogen.

3.4 Size Distribution of Nanoparticles

The size distribution of these Ag and Ni nanoparticles embedded within the polymer droplets was determined using PEBBLES, an image analysis software developed by Mondini et al.[63] Unlike other image analysis software (e.g., ImageJ), PEBBLES can be used to automatically measure the size distribution of nanoparticles within a low contrast medium (such as a polymer).[64] PEBBLES analyzes the intensity of pixels within a TEM micrograph and employs fitting algorithms that yield accurate and unbiased size distribution measurements. An example that illustrates the accuracy of these fitting algorithms is shown in Figure 3-14 (a). After data has been collected using PEBBLES, it can be statistically analyzed with a related program called PEBBLEJUGGLER. This additional program calculates the mean and median nanoparticle diameters and outputs size distribution histograms that can automatically be fitted to a log-normal curve. Figure 3-14 (b) shows an example of a size distribution histogram for the TEM image presented in Figure 3-14 (a). PEBBLES

and PEBBLEJUGGLER were used to understand how the variation of different process variables (e.g., polymer molecular weight, furnace temperature, etc.) would influence the size distribution and morphology of the synthesized nanoparticles.

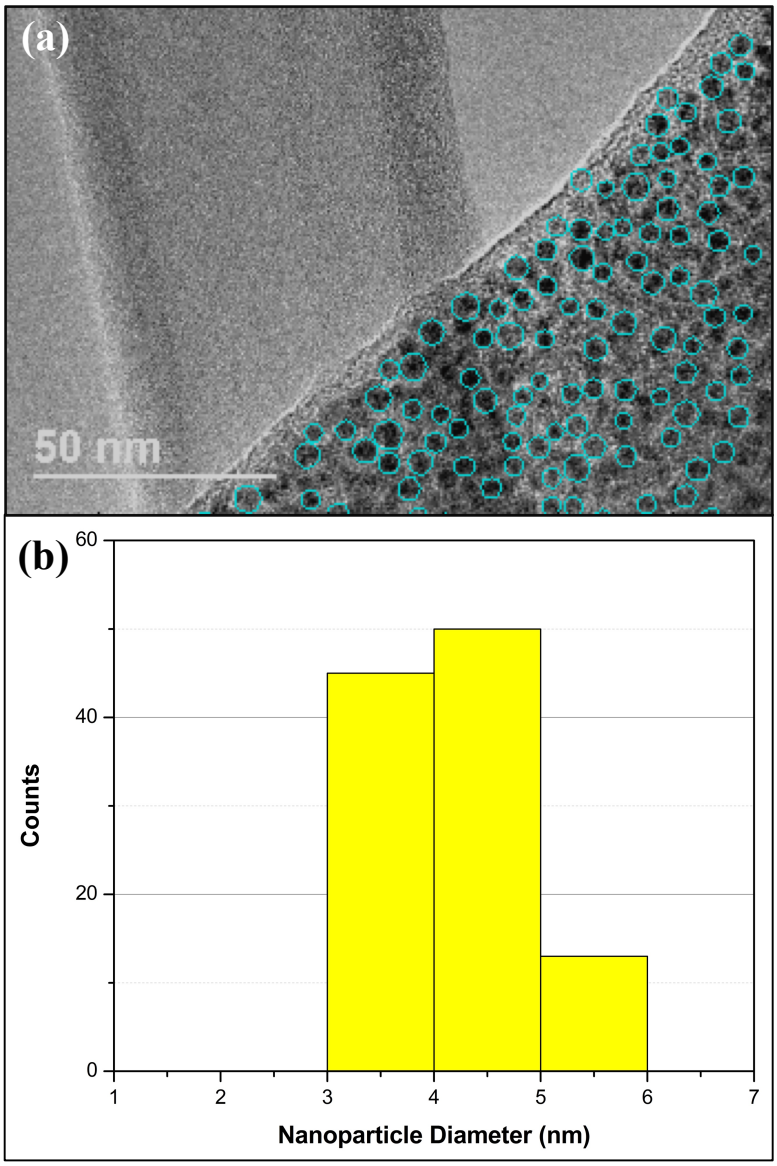

Figure 3-14: (a) TEM micrograph of a Ag-PVP sample analyzed using PEBBLES. **(b)** Histogram of the size distribution data obtained using PEBBLEJUGGLER.

Chapter 4: Data Analysis and Discussion

4.1 Variation of Metal Salt Precursor to Polymer Mass Ratio

The effect of decreasing the metal salt to polymer mass ratio in the ASP precursor solution was investigated for both the Ag and Ni polymer nanocomposite systems. As mentioned previously for the Ag-PVP system, it was observed that decreasing the metal salt concentration in the precursor solution yielded a thicker PVP coating around the spherical polymer droplets containing the Ag nanoparticles. This is highlighted in Figure 4-1 (a and b) for different polymer droplets synthesized from precursor solutions with 1 to 1 and 1 to 10 mass ratios of $AgNO_3$ to high molecular weight PVP (MW=1.3E6 g/mol). For this system, decreasing the metal salt concentration in the precursor solution yielded smaller Ag nanoparticles. As observed in Figure 4-2 (a), using a 1 to 1 mass ratio precursor solution produces Ag nanoparticles as large as 40 to 50 nm in diameter. However, when using a 1 to 3 or even a 1 to 10 mass ratio, the diameter of the Ag nanoparticles is reduced to 15 nm or less as shown in Figure 4-2 (b and c).

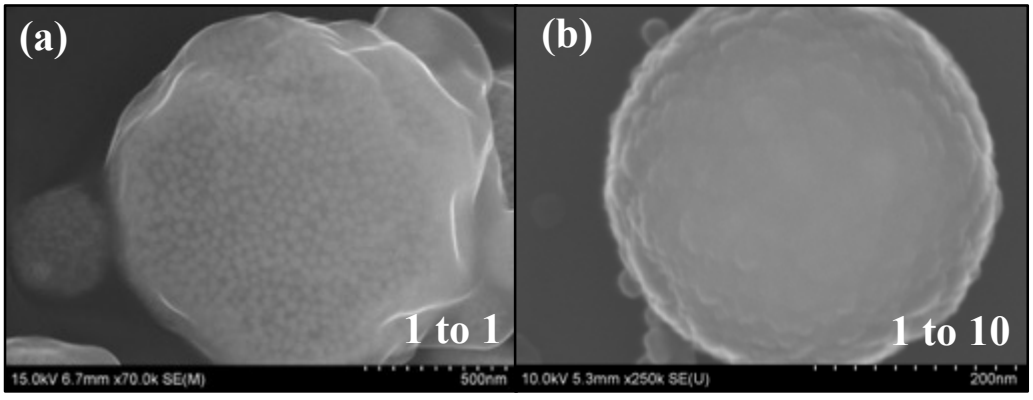

Figure 4-1: SEM micrographs of Ag-PVP samples prepared using **(a)** 1 to 1 and **(b)** 1 to 10 metal salt to polymer ($AgNO_3$ to PVP) mass ratio within the ASP precursor solution.

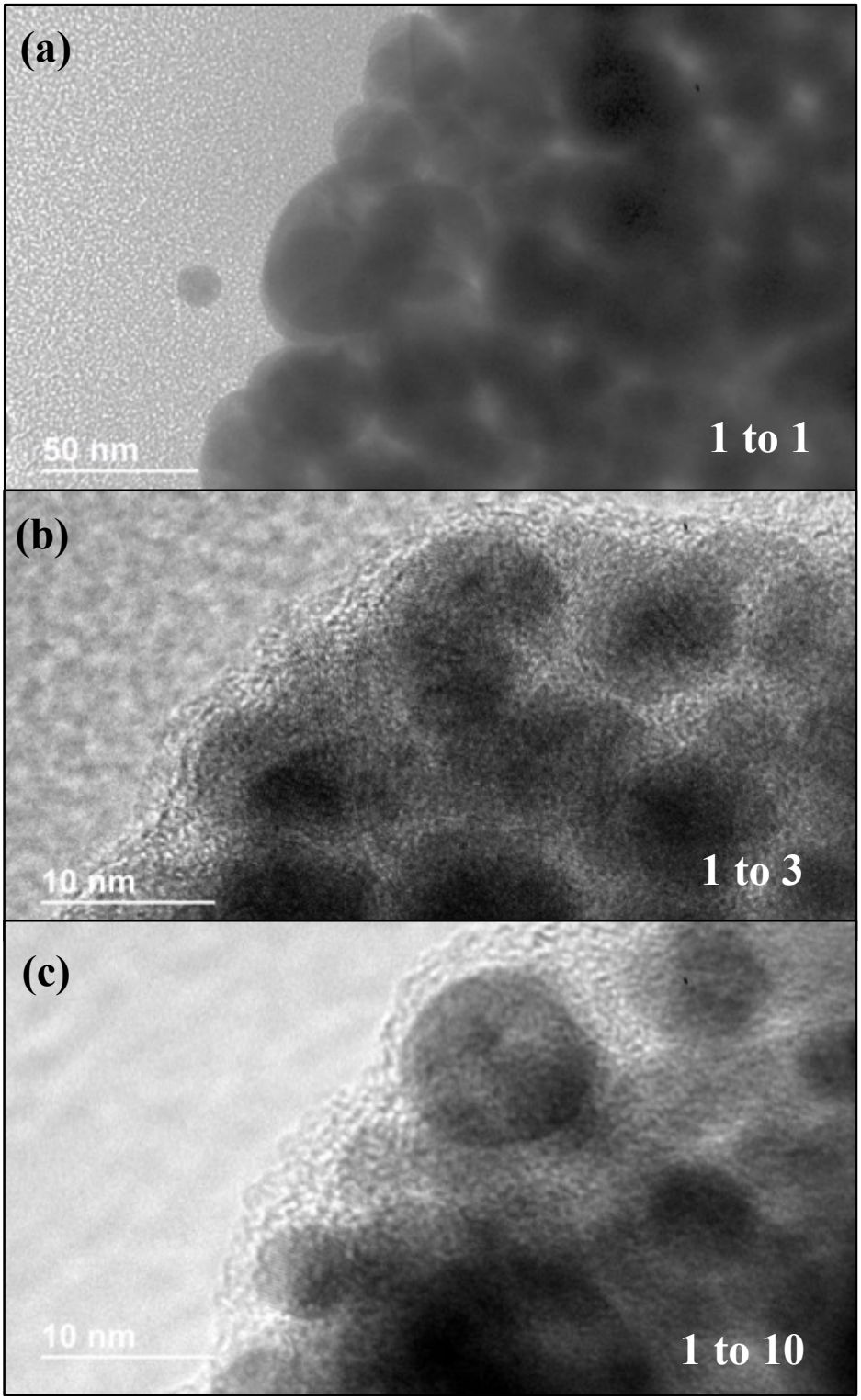

Figure 4-2: TEM micrographs of Ag-PVP samples prepared using **(a)** 1 to 1, **(b)** 1 to 3, and **(c)** 1 to 10 metal salt to polymer ($AgNO_3$ to PVP) mass ratios within the ASP precursor solution.

Upon varying the metal salt to polymer mass ratio in the Ni nanoparticle precursor solutions, the observed size distribution also underwent a notable change. For the Ni-PVP system, the initially non-uniform nanoparticles synthesized from a 1 to 1 metal salt to polymer mass ratio were observed to decrease in diameter and become monodisperse as the metal salt concentration in the precursor solution was reduced. This trend is illustrated in the TEM imagery presented in Figures 4-3 and 4-4. For the high molecular weight PVP system (MW=1.3E6 g/mol), nanoparticles synthesized from a 1 to 1 mass ratio had an average diameter of 6.5 nm that decreased to 3.5 nm when a 1 to 3 mass ratio was used. Similarly, the average diameter of Ni nanoparticles embedded within low molecular weight PVP (MW=8000 g/mol) decreased from 6 nm to 2.5 nm when the mass ratio was varied in this manner. As the metal salt concentration in the precursor solution was further reduced to obtain mass ratios of 1 to 10 and 1 to 25, the average diameter of the Ni nanoparticles did not decrease any further. This indicates that there is a critical mass ratio of 1 to 3 beyond which the size of Ni nanoparticles cannot be further reduced. This observed trend is graphically depicted in Figure 4-5.

Although decreasing the metal salt concentration in the precursor solution could imply that the number concentration of Ni nanoparticles within the polymer matrix should decrease, this was not observed experimentally. Figure 4-6 graphically depicts how the areal number density increases as the metal salt concentration in the precursor solution is lowered. This observation could stem from the increased decomposition of PVP molecules not adsorbed to the surface of the Ni nanoparticles as they pass through the tube furnace reactor in the ASP experiments. This proposed

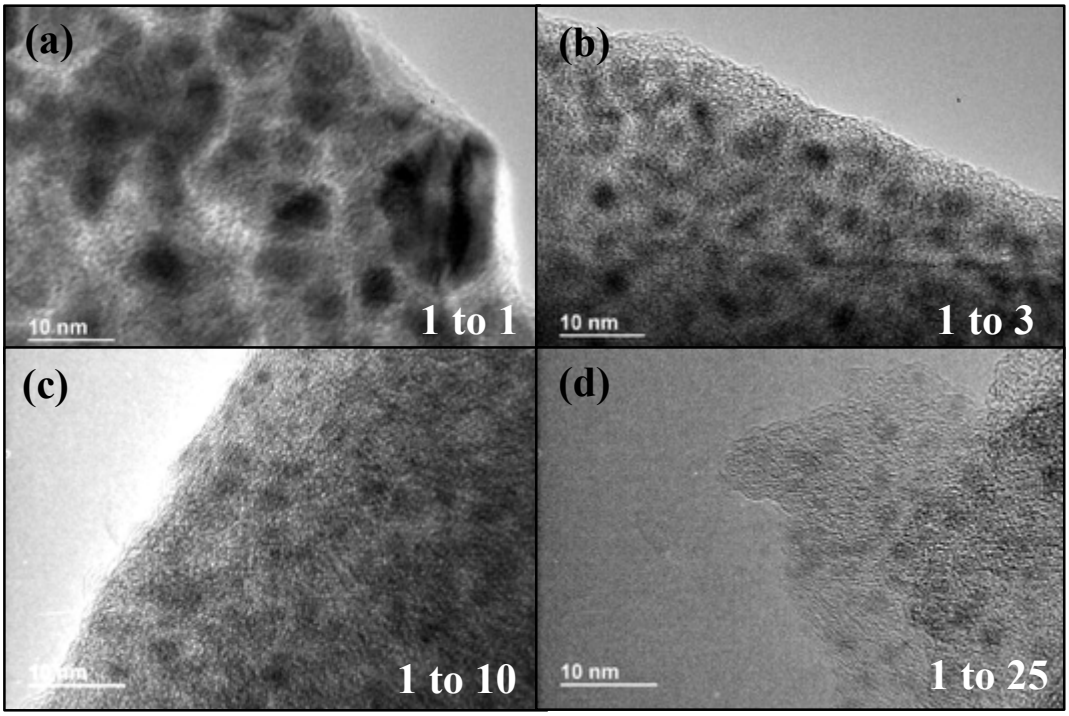

Figure 4-3: TEM micrographs of Ni-PVP (MW=1.3E6 g/mol) samples prepared using **(a)** 1 to 1, **(b)** 1 to 3, **(c)** 1 to 10, and **(d)** 1 to 25 metal salt to polymer ($NiNO_3 \cdot 6H_2O$ to PVP) mass ratios within the ASP precursor solution.

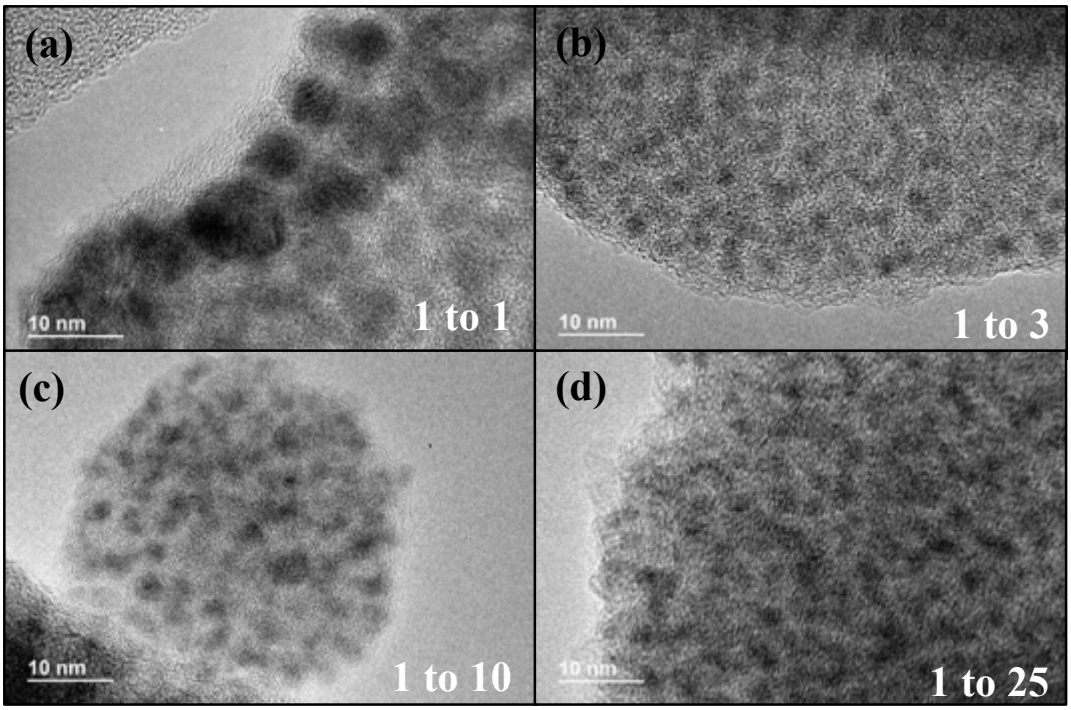

Figure 4-4: TEM micrographs of Ni-PVP (MW=8000 g/mol) samples prepared using **(a)** 1 to 1, **(b)** 1 to 3, **(c)** 1 to 10, and **(d)** 1 to 25 metal salt to polymer ($NiNO_3 \cdot 6H_2O$ to PVP) mass ratios within the ASP precursor solution.

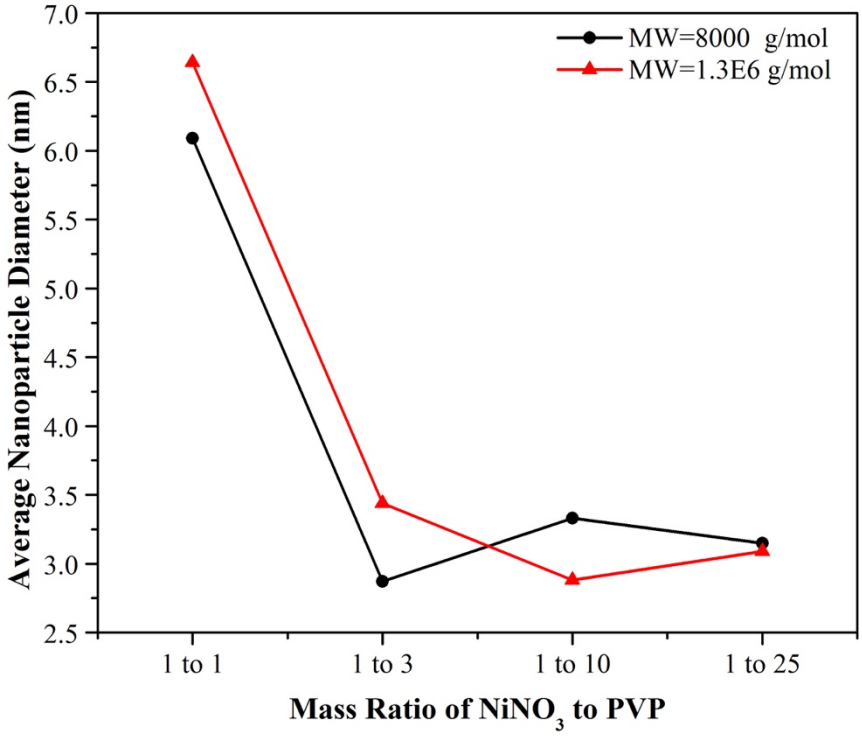

Figure 4-5: Plot of average nanoparticle diameter versus metal salt to polymer ($NiNO_3 \cdot 6H_2O$ to PVP) mass ratio within the ASP precursor solution.

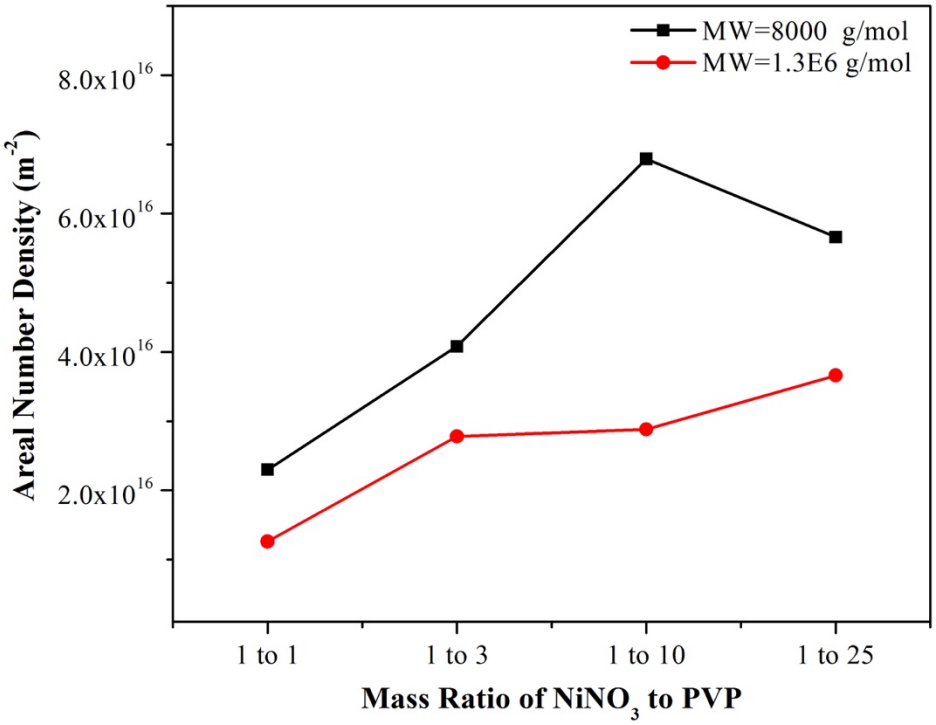

Figure 4-6: Plot of areal number density versus metal salt to polymer ($NiNO_3 \cdot 6H_2O$ to PVP) mass ratio within the ASP precursor solution.

explanation also supports why the sample yield notably decreases for ASP precursor solutions with lower metal salt concentrations (as shown in Figure 4-7). In other words, the total amount of particulate material collected on the filter paper used in the ASP apparatus was observed to be substantially less when higher mass ratios were used.

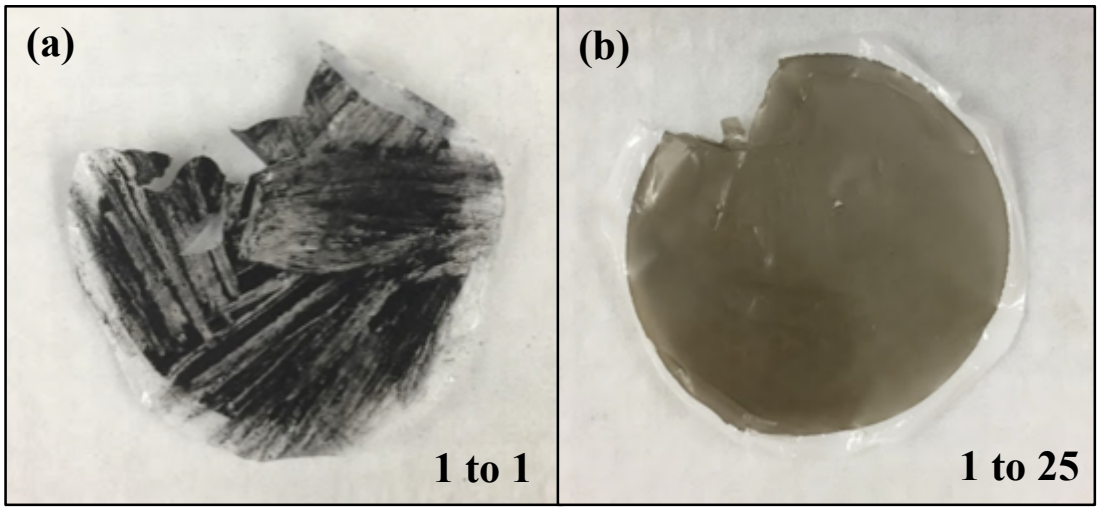

Figure 4-7: Photographs of Ni-PVP polymer nanocomposite samples synthesized using metal salt to polymer ($NiNO_3 \cdot 6H_2O$ to PVP) mass ratios of **(a)** 1 to 1 and **(b)** 1 to 25. The amount of sample collected on the filter paper substantially decreases when using higher mass ratios.

A notable change in the size distribution of Ni nanoparticles was also observed in the Ni-PEG system upon decreasing the concentration of $NiNO_3 \cdot 6H_2O$ within the precursor solution. As shown in Figure 4-8 (a), the Ni nanoparticles produced from a 1 to 1 metal salt to polymer mass ratio exhibited a bimodal size distribution with diameters ranging from 5 to 10 nm and 15 to 25 nm. Quantitatively, the 15 to 25 nm particles comprise approximately 15% of the total number of particles analyzed. Upon decreasing the metal salt precursor concentration to achieve

a 1 to 3 mass ratio, the Ni nanoparticles became monodisperse with diameters ranging from only 5 to 10 nm as shown in Figure 4-8 (b).

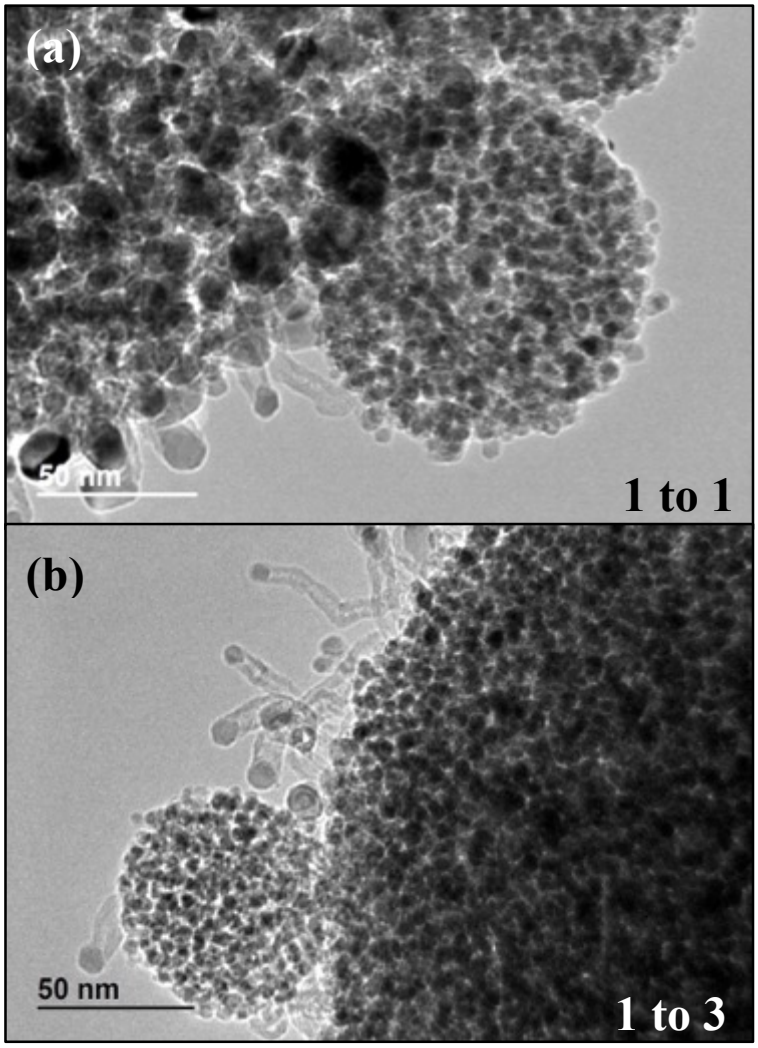

Figure 4-8: TEM micrographs of Ni-PEG samples prepared using **(a)** 1 to 1 and **(b)** 1 to 3 metal salt to polymer ($NiNO_3 \cdot 6H_2O$ to PEG) mass ratios within the ASP precursor solution.

The bimodal distribution of Ni nanoparticles observed in the Ni-PEG system for a 1 to 1 mass ratio could be caused by the thermal decomposition of PEG adhered to the surface of the Ni nanoparticles. TGA data reported in the literature demonstrate that the onset of thermal decomposition for PEG within an inert environment can

occur below 400˚C.[65,66] This contrasts with PVP which does not undergo substantial thermal degradation until 475˚C.[67] The greater thermal stability of PVP could prevent the growth of Ni agglomerates, contributing to the formation of a monodisperse size distribution when a 1 to 1 metal salt to polymer mass ratio is used. By lowering the metal salt concentration of the precursor solution, the bimodal size distribution observed in the Ni-PEG system can be made monodisperse. The excess polymer within the precursor solution can be used to form thicker PEG layers around the Ni nanoparticles, counteracting the ongoing thermal degradation. This process would naturally inhibit the diffusion of Ni nanoparticles within the polymer matrix and prevent the formation of agglomerates, yielding a monodisperse size distribution.

4.2 Carbon Nanotube (CNT) Formation

Within the Ni-PEG system, the formation of carbon nanotubes (CNTs) was observed. Ni is known to exhibit catalytic activity for decomposing carbon precursors and forming graphitic sheets since it has few d-vacancies in its electronic structure.[68,69] The pyrolysis of PEG using a Ni catalyst has been reported to promote CNT formation at temperatures ranging from 600˚C to 850˚C.[70] The ongoing thermal decomposition of PEG has been reported to yield organic peroxides which could adhere to the surface of Ni nanoparticles and be catalytically decomposed into pure carbon.[71] If the concentration of carbon atoms adhered to a particular Ni nanoparticle reaches supersaturation, a graphitic layer could form.[72] This graphitic layer could continue to grow until the ASP experiment is terminated, at which point there would no longer be a carbon source for promoting CNT growth. This growth mechanism,

illustrated in Figure 4-9, shows how carbon atoms can crystallize on the Ni nanoparticle's surface to yield the CNTs observed in Figure 4-8 (b).[73]

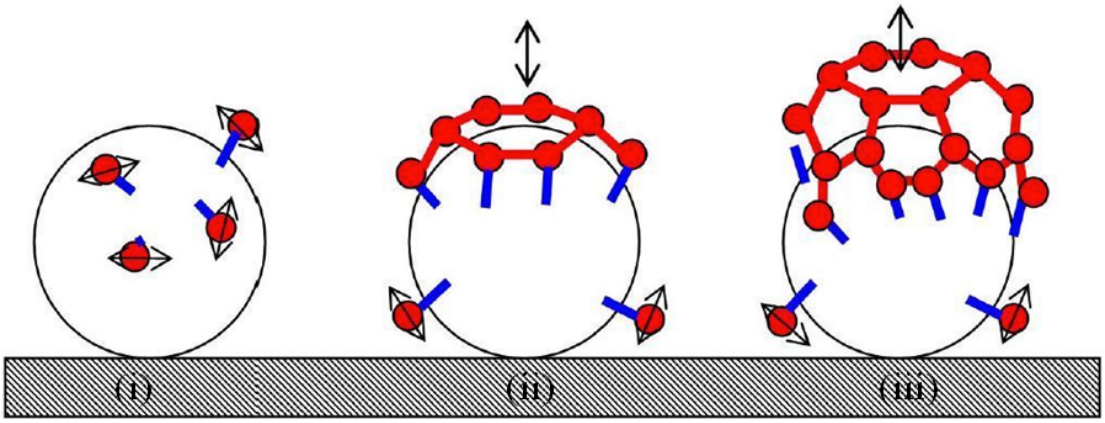

Figure 4-9: Schematic of CNT growth on a metal catalyst, as observed in ab initio simulations. **(i)** Diffusion of single C atoms (red spheres) on the surface of the catalyst. **(ii)** Formation of graphene sheet on catalyst surface with edge atoms covalently bonded to the metal. **(iii)** Root incorporation of diffusing single C atoms. Reprinted from Chapter 8 of Mukul Kumar (2011). Carbon Nanotube Synthesis and Growth Mechanism, Carbon Nanotubes - Synthesis, Characterization, Applications, Dr. Siva Yellampalli (Ed.). Published by InTech under CC BY-NS-SA 3.0 license. Available from http://dx.doi.org/10.5772/19331. Full terms found at https://creativecommons.org/licenses/by-nc-sa/3.0/legalcode.[73]

4.3 Variation of Residence Time

To understand how changing the aerosol's residence time might affect nanoparticle growth, I conducted a quenching experiment. Instead of collecting particles at the end of the tube furnace using a filtration mechanism, I designed a cold finger to collect particles in the middle of the tube furnace. By maintaining an aluminum substrate at a cool temperature, I established a temperature gradient between the collector and its surrounding environment to collect particles via thermophoresis. Using this approach, I quenched the system while also reducing the residence time of the particles from 6.48 seconds to 3.24 seconds. The SEM micrographs presented in Figure 4-10 illustrate how increasing the mass ratio of the

Ag-PVP system still yielded a thicker coating of PVP around the Ag nanoparticles regardless of the change in residence time. However, the TEM micrographs presented in Figure 4-11 reveal how using a shorter residence time and quenching mechanism drastically modified the Ag nanoparticle size distribution and inter-particle spacing for Ag-PVP systems prepared using high metal salt to polymer mass ratios within the ASP precursor solution. These TEM micrographs illustrate how the size distribution of Ag nanoparticles synthesized using a 1 to 1 mass ratio has been substantially reduced from 20 to 30 nm in diameter down to 5 to 10 nm in diameter by using a 1 to 25 mass ratio.

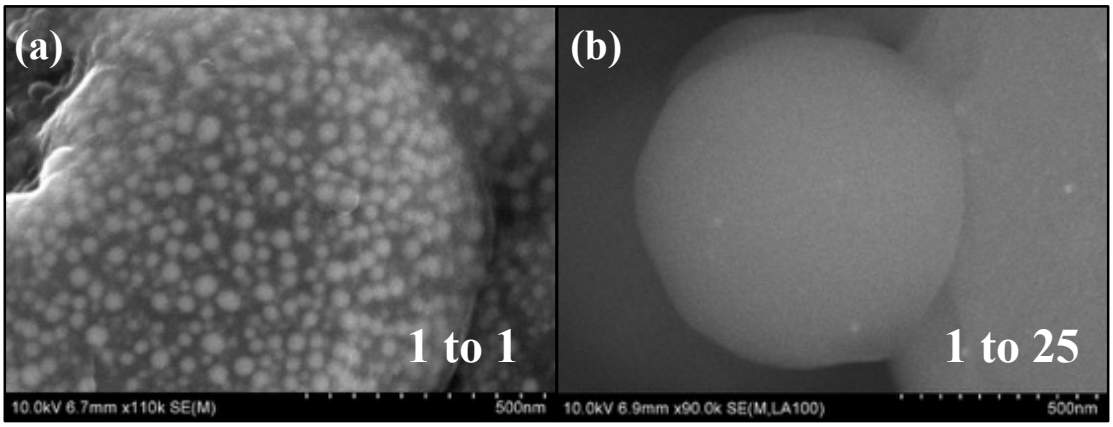

Figure 4-10: SEM micrographs of Ag-PVP samples collected using a cold finger and prepared using **(a)** 1 to 1 and **(b)** 1 to 25 metal salt to polymer ($AgNO_3$ to PVP) mass ratios within the ASP precursor solution.

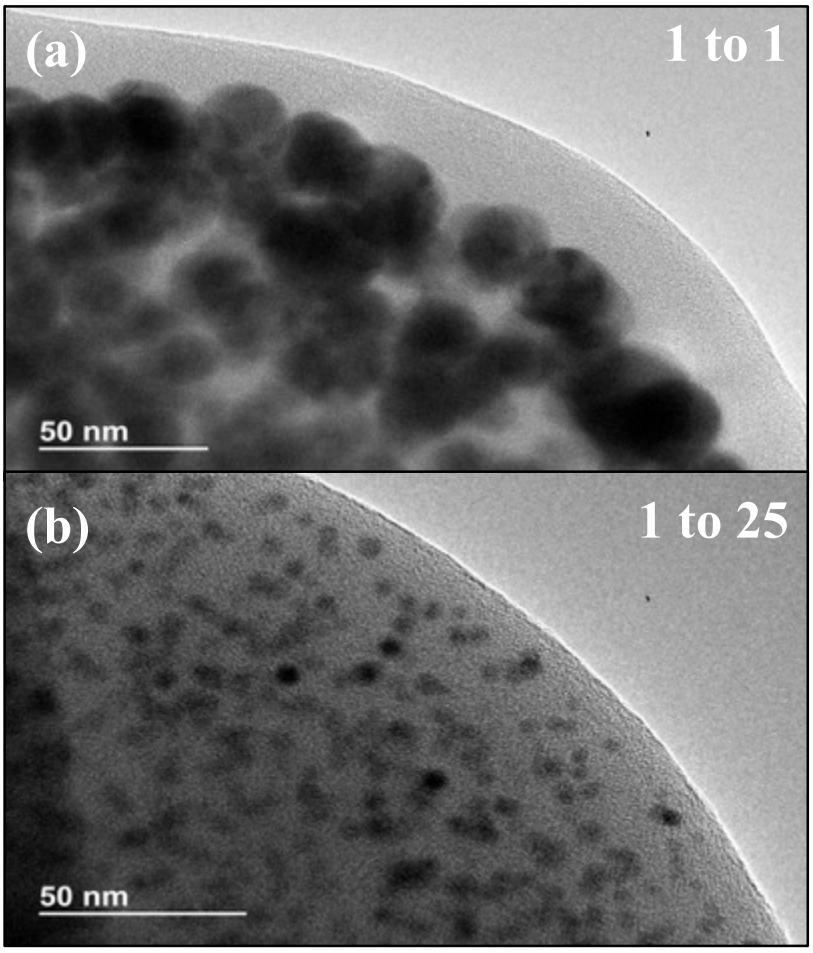

Figure 4-11: TEM micrographs of Ag-PVP samples collected using a cold finger and prepared using **(a)** 1 to 1 and **(b)** 1 to 25 metal salt to polymer ($AgNO_3$ to PVP) mass ratios within the ASP precursor solution.

As an alternative to the cold finger, the residence time of the particles within the tube furnace was varied by changing the carrier gas flow rate within my ASP experiments. For the Ni-PEG system, the flow rate of the 5% H_2 and 95% N_2 carrier gas mixture was increased from 3 LPM to 6 LPM to reduce the residence time of the particles from 6.48 seconds to 3.24 seconds. These nanoparticles were collected at the end of the tube furnace using filter paper. As shown in Figure 4-12, nanoparticles synthesized using a shorter residence time of 3.24 seconds were observed to be

monodisperse with an average diameter of 5.5 nm while nanoparticles synthesized using a longer residence time of 6.48 seconds were observed to be bimodal with an average diameter of 8.2 nm.

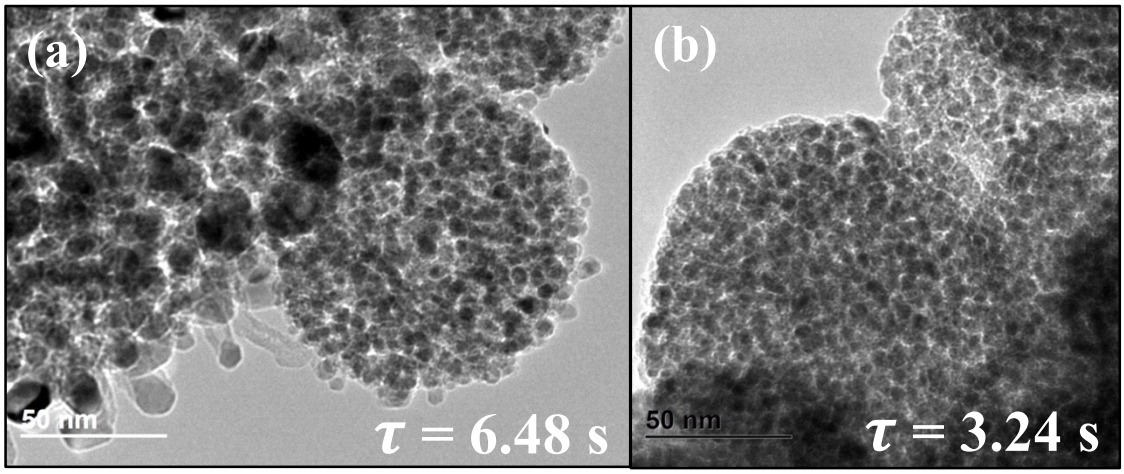

Figure 4-12: TEM micrographs of Ni-PEG samples synthesized via ASP using residence times (τ) of **(a)** 6.48 seconds and **(b)** 3.24 seconds. Both samples were synthesized using a 1 to 1 metal salt to polymer ($NiNO_3 \cdot 6H_2O$ to PEG) mass ratio within the ASP precursor solution.

4.4 Effect of Temperature

Within this study, the tube furnace temperature was also investigated as a process variable for controlling nanoparticle growth. For many of the systems investigated within this work, higher temperatures yielded larger nanoparticles. For the synthesis of Ni nanoparticles within a PVP matrix using a precursor solution with the critical metal salt to polymer mass ratio of 1 to 3, a notable increase in nanoparticle size was observed when the tube furnace temperature was raised from 600˚C to 800˚C. This observed trend is illustrated in the TEM imagery presented in Figure 4-13. The Ni nanoparticles synthesized at 800˚C are observed to be polydisperse and have diameters ranging from 5 to 25 nm, whereas the Ni nanoparticles synthesized at 600˚C are monodisperse with an average diameter of 3.5

nm. Since the viscosity of PVP is expected to decrease as the temperature of the tube furnace is increased, the larger agglomerates observed at 800˚C have possibly been formed by the enhanced coagulation of Ni nanoparticles diffusing through the polymer matrix.[74]

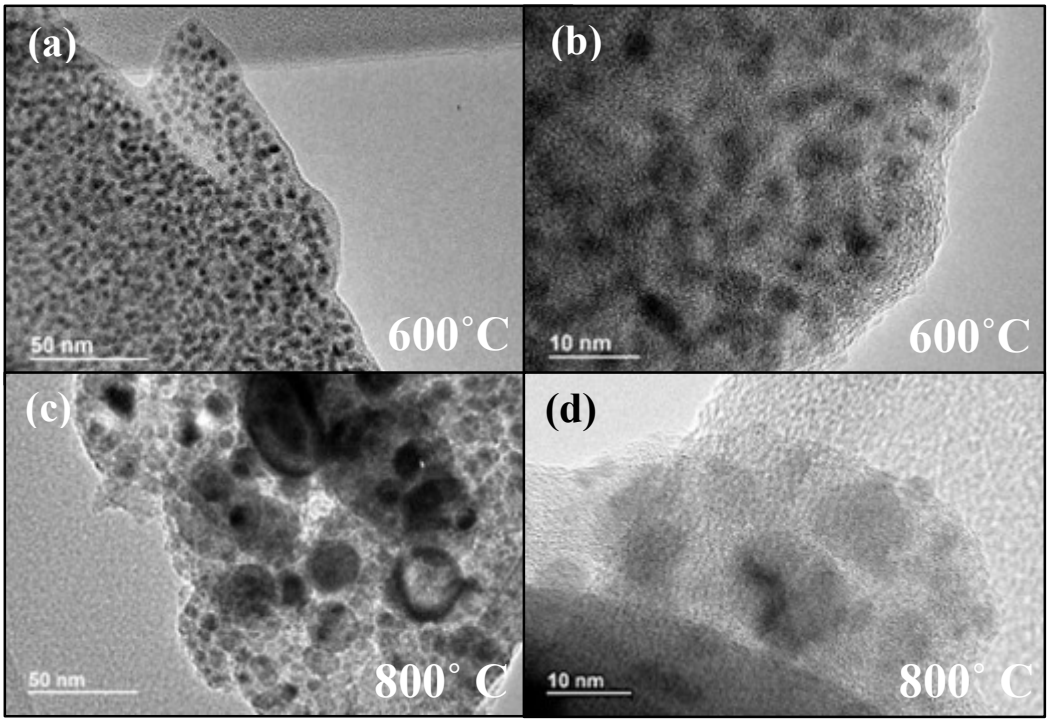

Figure 4-13: TEM micrographs of Ni-PVP samples synthesized at **(a) and (b)** 600˚C and **(c) and (d)** 800˚C prepared using a 1 to 3 metal salt to polymer ($NiNO_3 \cdot 6H_2O$ to PVP) mass ratio within the ASP precursor solution.

As the temperature of the tube furnace reactor was lowered from 600˚C to 400˚C, the nanoparticles synthesized from a 1 to 1 mass ratio of $NiNO_3 \cdot 6H_2O$ to PEG or PEO also underwent a change in size. As mentioned previously, the Ni nanoparticles synthesized at 600˚C and encapsulated within PEG are observed to have a bimodal size distribution ranging from 5 to 10 nm and 15 to 25 nm. Upon decreasing the furnace temperature to 400˚C, the nanoparticle size distribution becomes much narrower and the average diameter of the nanoparticles is observed to

decrease to 5 nm as seen in Figure 4-14 (c). This trend was also observed for the Ni-PEO system. Figure 4-14 (d) shows that upon decreasing the tube furnace temperature to 400˚C for the Ni-PEO system, the nanoparticles become monodisperse with diameters ranging between 2 to 4 nm. The XRD data presented in Figure 4-15, however, demonstrate that these extremely small nanoparticles could not be confirmed to be pure Ni.

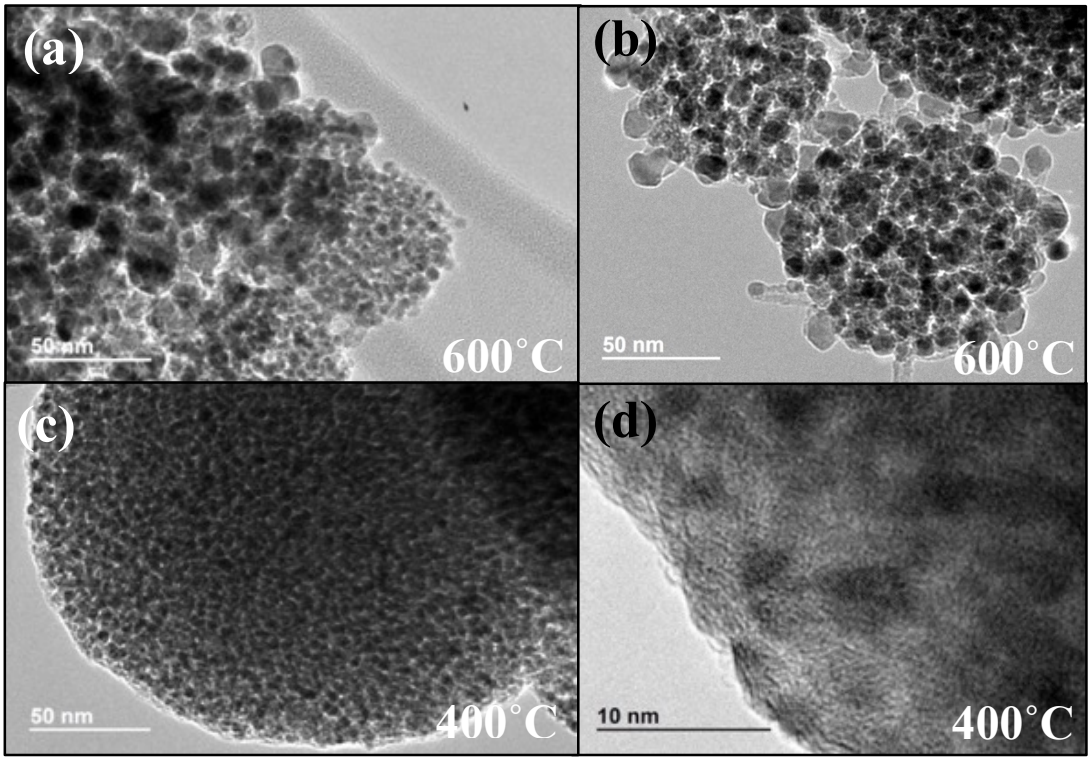

Figure 4-14: TEM micrographs of (**a) and (c)** Ni-PEG samples synthesized at 600˚C and 400˚C, respectively, and **(b) and (d)** Ni-PEO samples synthesized at 600˚C and 400˚C, respectively. All samples were synthesized using a 1 to 1 metal salt to polymer ($NiNO_3 \cdot 6H_2O$ to PEG or PEO) mass ratio within the ASP precursor solution.

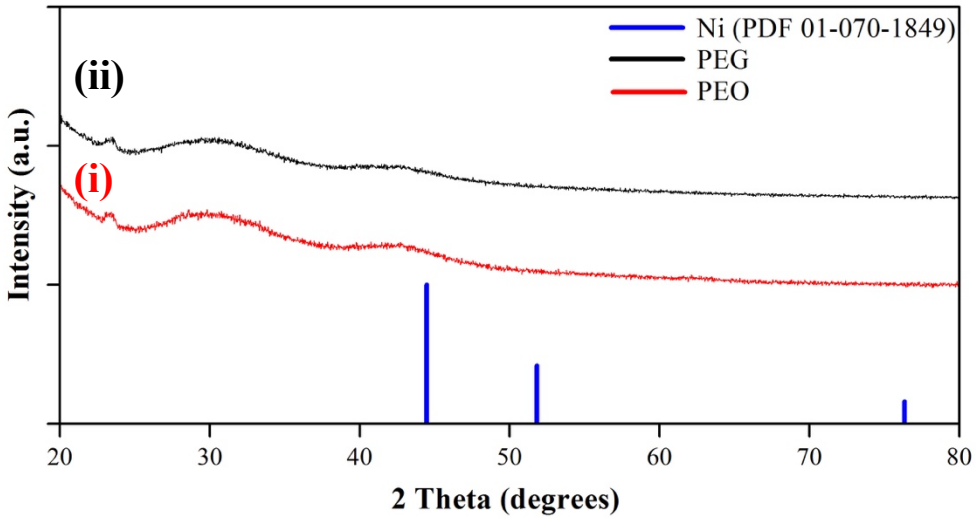

Figure 4-15: XRD data collected for nanoparticles synthesized using an ASP precursor solution of $NiNO_3 \cdot 6H_2O$ and (i) PEO or (ii) PEG at 400˚ C. This data demonstrates the extremely small nanoparticles observed in Figure 4-14 (c) and (d) cannot be confirmed to be Ni.

The temperature of the tube furnace was also varied for the Ni-PEG experiments in which the carrier gas flow rate was increased to reduce the residence time from 6.48 seconds to 3.24 seconds. Figure 4-16 shows the TEM micrographs and size distribution histograms of nanoparticles synthesized at these varying temperatures using a shorter residence time. The mean nanoparticle diameter was measured to be 3.4 nm, 5.5 nm, and 7.2nm for 400˚C, 600˚C, and 800˚C respectively. The XRD data presented in Figure 4-17, however, indicates that only nanoparticles synthesized at 800˚C using this shorter residence time were confirmed to be pure Ni.

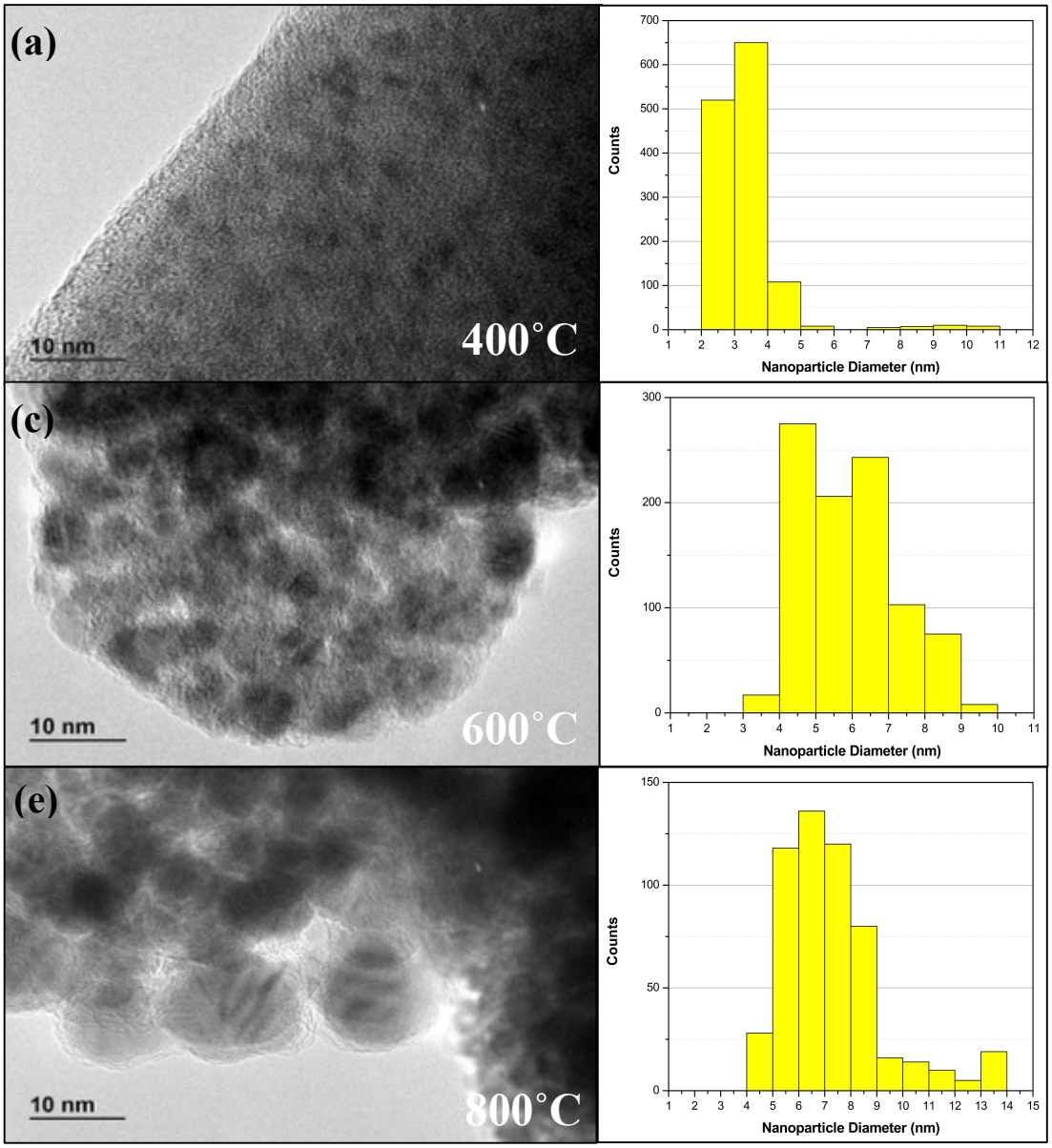

Figure 4-16: TEM micrographs and size distribution histograms of Ni-PEG samples synthesized at **(a) and (b)** 400˚C, **(c) and (d)** 600˚C, and **(e) and (f)** 800˚C using a shorter residence time of 3.24 seconds.

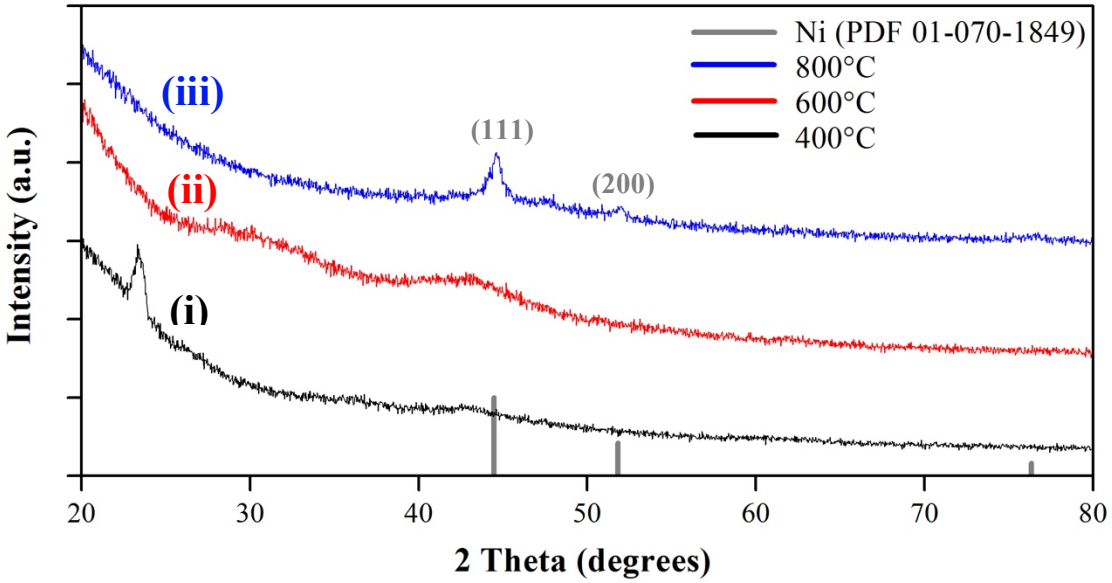

Figure 4-17: XRD data collected for Ni-PEG samples synthesized at **(i)** 400˚C, **(ii)** 600˚C, and **(iii)** 800˚C using a shorter residence time of 3.24 seconds. This data indicates that pure Ni nanoparticles were obtained only at 800˚C when using a shorter residence time.

4.6 Variation of Polymer Molecular Weight

To investigate how the length of a polymer chain might affect the nanoparticle size distribution, polymers with different molecular weights were introduced into the ASP precursor solutions. For the Ag-PVP system, the use of lower molecular weight PVP (MW=8000 g/mol) was observed to produce smaller Ag nanoparticles than higher molecular weight PVP (MW=1.3E6 g/mol). As shown in Figure 4-18, Ag nanoparticles have been reduced in size from approximately 10 to 12 nm down to 3 to 5 nm by decreasing the molecular weight of PVP by three orders of magnitude. This observation does not agree with the results of Lee et al. who claim that smaller nanoparticles could be obtained using higher molecular weight PVP.[49] Lee et al. suggest that since the concentration of PVP in the precursor solution was kept constant regardless of which molecular weight PVP was being used, there should be

more lower molecular weight PVP chains available to coagulate and create large molecular aggregates that would lead to the formation of bigger Ag nanoparticles. This explanation, however, fails to address why higher molecular weight PVP chains would not also coagulate to yield even larger Ag aggregates.

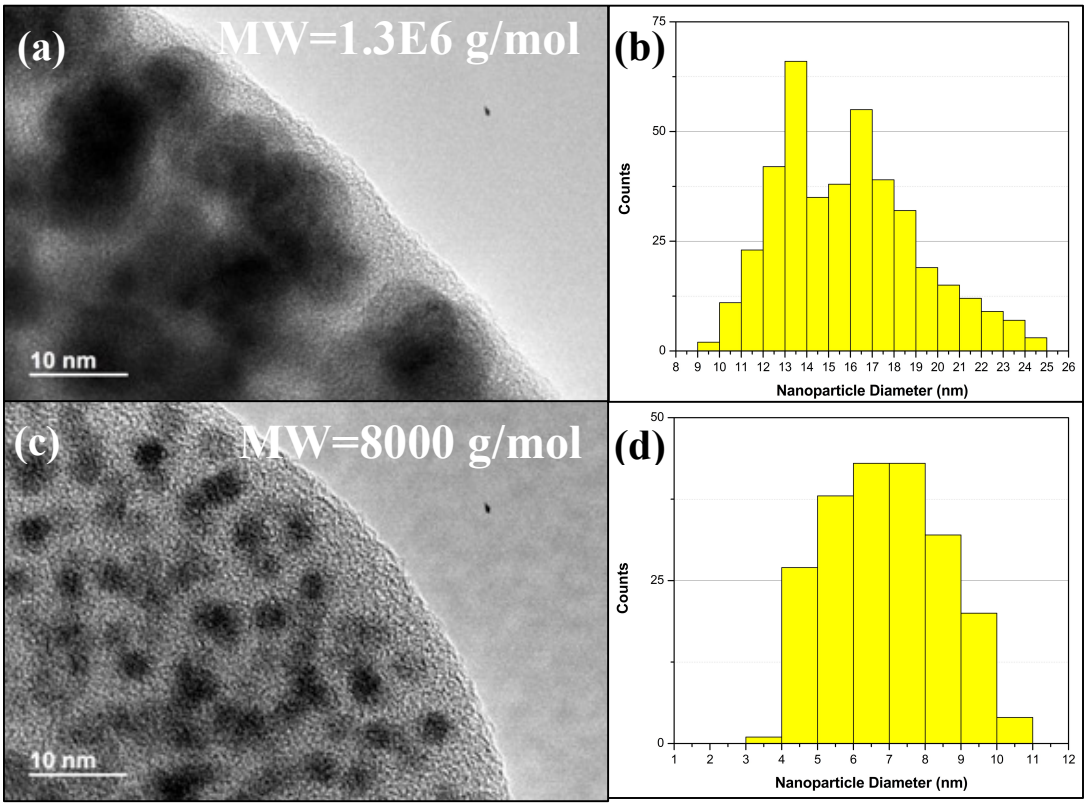

Figure 4-18: TEM micrographs and size distribution histograms of Ag-PVP samples synthesized using different molecular weight PVP within the ASP precursor. **(a) and (b)** MW=1.3E6 g/mol; **(c) and (d)** MW=8000 g/mol.

This observed trend might relate to a change in the rheological properties associated with varying the molecular weight of PVP. If the growth of Ag nanoparticles is primarily driven by the diffusion of nanoclusters within the PVP matrix, the formation of aggregates could ultimately be controlled by the viscosity of the polymer medium. The diffusivity of these nanoclusters should be related to the viscosity of the polymer medium by the Stokes-Einstein equation:

$$D = \frac{k_B T}{3\pi\eta d}$$

where k_B is the Boltzmann constant, T is the absolute temperature, d is the particle's diameter, and η is the viscosity of the polymer.[75] Experiments have shown that the zero-shear viscosity (η_0) of a polymer melt scales with molecular weight in the following manner:

$$\eta_0 = k_0 M_w \quad \text{for } M_w < M_{crit}$$

$$\eta_0 = k_0 M_w^{3.5} \text{ for } M_w > M_{crit}$$

where k_0 is a constant, M_w is the molecular weight of the polymer, and M_{crit} is the critical average molecular weight at which molecular entanglement dominates the slippage rate of molecules.[74] These equations demonstrate that the viscosity of a polymer melt should increase with molecular weight. According to the Stokes-Einstein equation, higher molecular weight polymer melts should retard the diffusion of Ag nanoclusters. However, the observed formation of larger Ag aggregates within the higher molecular weight PVP suggests that the zero-shear viscosity of the polymer melt cannot be used to reliably assess the diffusivity of these metallic nanoclusters.

Within polymer melts, evaluating the diffusivity of metal nanoparticles has been shown to depend on the ratio of the nanoparticle's radius (R_{NP}) to the polymer chain's radius of gyration (R_g).[76] For cases in which $R_{NP} > R_g$, nanoparticle diffusivity can be predicted accurately using the Stokes-Einstein equation. When $R_{NP} < R_g$, however, the diffusivity of nanoparticles can no longer be described using hydrodynamic motion and the polymer melt's macroscopic viscosity becomes

irrelevant.[77] Within this size regime, the frictional force exerted on the particle notably decreases because the particle is smaller than the entanglement mesh size (the average distance between neighboring polymer chains). The primary frictional force exerted on the particle results from the physical contact taking place between the particle and any adjacent monomer. Thus, particle motion is now governed by a local viscosity that is proportional to the particle's surface area (R_{NP}^2).[77–79] Unlike the macroscopic viscosity of a polymer melt, this local viscosity does not vary with the polymer system's molecular weight.

Since Ag nanocluster formation is not controlled by the viscosity of the polymer melt, it is conjectured that larger Ag aggregates are formed within higher molecular weight PVP because longer polymer chains exhibit a greater excluded volume than shorter polymer chains. When polymers are heated above their theta temperature, steric effects between monomers can lead to repulsive interactions. The entanglement of polymer chains with higher degrees of polymerization will therefore create wider gaps of space between polymer chains, enabling the formation of larger Ag aggregates within higher molecular weight polymer systems. Varying the molecular weight of polymers used within the $NiNO_3 \cdot 6H_2O$ precursor solutions, however, did not lead to any substantial changes in the observed nanoparticle size distribution.

4.7 Proposed Mechanisms for Nanoparticle Growth

To better understand whether the underlying process for nanoparticle growth might be driven by the coagulation of particles within the polymer matrix, the measured size distribution for each polymer nanocomposite system was compared to

the self-preserving particle size distribution.[80] The asymptotic behavior of an initially monodisperse system undergoing coagulation can be observed at long times using a similarity transformation that makes the distribution time invariant. This self-preserving distribution can be approximated with a lognormal distribution function in which the geometric standard deviation (σ_g) will equal 1.44 for the continuum regime and 1.46 for the free molecular flow regime. A particle size distribution has become self-preserving if it has a σ_g value that lies within 1% of these self-preserving values.[81] As presented in Table 4-1, the lognormal distribution functions fitted to the particle size distribution data acquired with PEBBLES did not exhibit σ_g values that fell within 1% of the σ_g values characteristic of a self-preserving distribution. While this might indicate that coagulation is not the primary mechanism for nanoparticle growth, it is also possible that these size distributions did not reach a self-preserving state because of the limited residence time of particles within the tube furnace.

Polymer Nanocomposite System	Metal Salt to Polymer Mass Ratio	Furnace Temperature (˚C)	Molecular Weight (g/mol)	Geometric Standard Deviation (nm)
Ag-PVP	1 to 3	400	8000	**1.269**
Ag-PVP	1 to 3	400	1.30E+06	**1.218**
Ni-PVP	1 to 3	600	1.30E+06	**1.217**
Ni-PEG	1 to 1	600	8000	**1.234**
Ni-PEO	1 to 1	600	600,000	**1.228**

Table 4-1: σ_g values calculated from the lognormal distribution functions fitted to the particle size distribution data of different polymer nanocomposite systems.

The underlying mechanisms believed to control the formation of monodisperse nanoparticles within the polymer nanocomposite systems presented above include: (i) the clustering of polymer chains, (ii) the diffusion of metal atoms through defects within a polymer melt, (iii) heterogeneous nucleation, and (iv) Ostwald ripening.[82] During the ASP experiment, the precursor solution is atomized to form droplets that will pass through the tube furnace reactor. In a high temperature environment, polymer chains will either melt or thermally decompose. Although TGA data of PVP, PEG, and PEO demonstrate that these polymers should fully decompose at temperatures above 475˚C, this was not observed in any of my ASP experiments.[66,67] This indicates that despite the high temperature within the tube furnace, the kinetics of decomposition are slow relative to the residence time. At high temperatures, these polymer chains can become entangled as they pass through the tube furnace, forming a polymer melt comprised of amorphous domains. As shown in Figure 4-19, a non-crystalline domain within a polymer can exhibit various types of structural defects (e.g., folds, twists, and kinks), contributing to the formation of larger vacancies between polymer chains through which metal atoms or small clusters can diffuse.[83,84] The surface of a polymer chain within a polymer melt can serve as a preferential site for the heterogeneous nucleation of metal nanoclusters. The heterogeneous nucleation and growth of such nanoclusters is expected to proceed as metal atoms continue diffusing through the polymer melt until they are stabilized via Ostwald ripening.

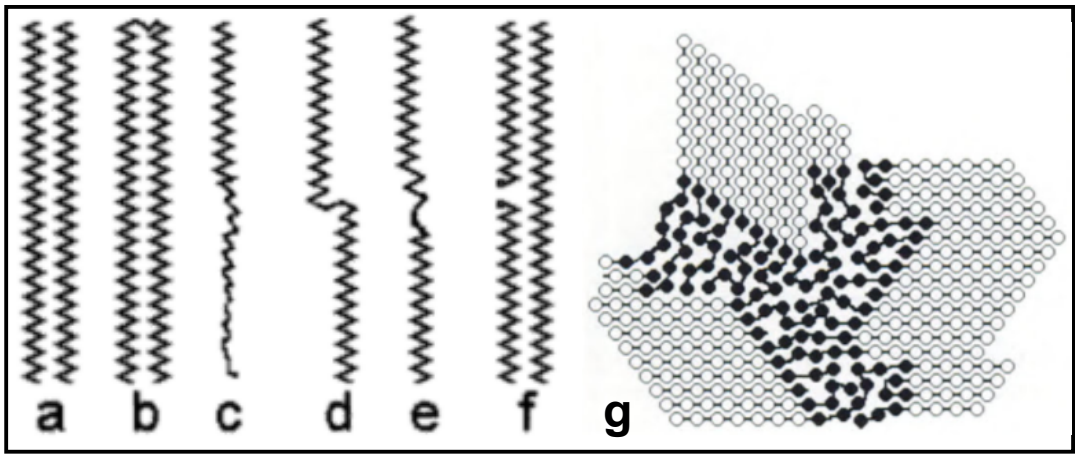

Figure 4-19: Schematic illustration of **(a)** defect-free polymer chains and polymer chains exhibiting different structural defects such as **(b)** folds, **(c)** twists, **(d)** jogs, **(e)** kinks, and **(f)** ends. The illustration presented in **(g)** demonstrates that such defects can lead to a loss in crystallinity within the polymer system. Republished with permission of Springer-Verlag Berlin Heidelberg from Wunderlich, B. Thermal Analysis of Polymeric Materials. Copyright © 2005.[84]

Chapter 5: Conclusion

5.1 Summary

In this work, aerosol spray pyrolysis (ASP) was used to generate metallic nanoclusters of less than 20 nm in diameter by incorporating a water-soluble polymer into a metal salt precursor solution. To tune the morphology of these nanoclusters, the following process variables were investigated: the mass ratio of the metal salt to polymer within the ASP precursor solution, the tube furnace reactor temperature, the carrier gas flow rate, and the polymer system's molecular weight. For the Ag-PVP, Ni-PVP, and Ni-PEG/PEO polymer nanocomposite systems, it was observed that decreasing the metal salt to polymer mass ratio within the ASP precursor solutions yielded smaller metallic nanoparticles. In the Ag-PVP system, for example, Ag nanoparticles with diameters of 40 to 50 nm produced using a 1 to 1 mass ratio were reduced to 15 nm or less by using a 1 to 3 mass ratio. Within the Ni-PVP system, a critical mass ratio of 1 to 3 was observed to yield extremely small Ni nanoclusters with diameters of 2 to 4 nm. The TEM micrographs acquired for these polymer nanocomposite systems show that the areal number density of the metallic nanoclusters generated within the polymer matrix does not notably decrease as the metal salt concentration is lowered within the ASP precursor solution. However, Ag nanoclusters synthesized with a 1 to 25 mass ratio and collected using a cold finger appear to exhibit greater inter-particle spacing that is concurrent with the size reduction of Ag nanoparticles. Other process variables such as the tube furnace temperature and carrier gas flow rate were studied to determine the optimal parameters for fully decomposing the metal salt precursor while also minimizing the

size of the generated nanoclusters. Upon varying the polymer system's average molecular weight within the Ag-PVP system, the size distribution of nanoparticles was observed to change substantially. The use of low molecular weight PVP (MW=8000 g/mol) yielded small Ag nanoclusters with diameters ranging from 3 to 5 nm while the use of high molecular weight PVP (MW=1.3E6 g/mol) generated larger Ag nanoclusters with diameters ranging from 10 to 12 nm.

For my ASP experiments, I conclude that the formation and growth of metal nanoparticles within a polymer matrix are controlled by the following mechanisms: (i) the clustering of polymer chains, (ii) the diffusion of metal atoms through defects within a polymer melt, (iii) heterogeneous nucleation, and (iv) Ostwald ripening. Upon generating an aerosol from a precursor solution comprised of a metal salt and a water-soluble polymer, the aerosol can be passed through a high-temperature tube furnace. This high-temperature environment will promote polymer chain clustering within each nebulized droplet and form a polymer melt comprised of amorphous domains through which metal atoms can diffuse and heterogeneously nucleate. The growth and stabilization of these nucleated nanoclusters is controlled by the process of Ostwald ripening, yielding a system of monodisperse metallic nanoclusters. As shown in my experimental results, these mechanisms ultimately contribute to the growth and stabilization of monodisperse Ag and Ni nanoclusters encapsulated within different polymer matrices.

5.2 Future Work

My efforts to grow and stabilize metal nanoclusters within a polymer matrix using ASP can be expanded upon to develop new strategies for synthesizing novel polymer nanocomposite materials. For example, the incorporation of branched or cross-linked polymers into the ASP precursor solution could be studied to determine if different polymer structures can be used to manipulate the shape and size distribution of the generated nanoclusters. Moreover, the incorporation of co-polymer chains and additional organic ligands could be investigated to promote the formation of nanoclusters within different parts of the polymer matrix (as demonstrated by Luo et al.).[13] Additionally, the incorporation of thermal free radical initiators alongside specific monomers within the ASP precursor solution could potentially enable one to arrest nanoparticle growth using a live polymerization reaction. In this manner, ASP has been used to generate microporous materials known as metal-organic frameworks (MOFs).[85] The pores of this polymeric matrix are uniformly distributed and can be modified both physically and chemically to enable bonding with various types of metal nanoparticles. When MOF synthesis requires precursors that must be dissolved in two different immiscible solvents, a three fluid atomizer (two fluids and one gas) can be used to ensure micro-droplets formed during atomization contain both precursors for the reaction to proceed. By exploring these different techniques while also analyzing the effect of other process variables such as a polymer's tacticity, glass transition temperature, and molar concentration within the ASP precursor solution, new correlations can be discovered to help facilitate the design of innovative polymer nanocomposite materials.

Bibliography

1. Pankhurst, Q. a., Thanh, N. T. K., Jones, S. K. & Dobson, J. Progress in applications of magnetic nanoparticles in biomedicine. *J. Phys. D. Appl. Phys.* **42,** 224001 (2009).
2. Olson, J. *et al.* Optical characterization of single plasmonic nanoparticles. *Chem. Soc. Rev.* **44,** 40–57 (2015).
3. Zaera, F. Shape-Controlled Nanostructures in Heterogeneous Catalysis. *ChemSusChem* **6,** 1797–1820 (2013).
4. Domenech, B. *et al.* in *Ion Exchange Technologies* 35–72 (InTech, 2012). doi:10.5772/51579
5. Choi, J., Shin, H., Yang, S. & Cho, M. The influence of nanoparticle size on the mechanical properties of polymer nanocomposites and the associated interphase region: A multiscale approach. *Compos. Struct.* **119,** 365–376 (2014).
6. Kutvonen, A., Rossi, G., Puisto, S. R., Rostedt, N. K. J. & Ala-Nissila, T. Influence of nanoparticle size, loading, and shape on the mechanical properties of polymer nanocomposites. *J. Chem. Phys.* **137,** 214901 (2012).
7. Zaragoza, J. *et al.* Experimental Investigation of Mechanical and Thermal Properties of Silica Nanoparticle-Reinforced Poly(acrylamide) Nanocomposite Hydrogels. *PLoS One* **10,** e0136293 (2015).
8. Sygletou, M. *et al.* Laser induced nucleation of plasmonic nanoparticles on two-dimensional nanosheets for organic photovoltaics. *J. Mater. Chem. A* **4,** 1020–1027 (2016).
9. Wu, H. *et al.* Stable Li-ion battery anodes by in-situ polymerization of conducting hydrogel to conformally coat silicon nanoparticles. *Nat. Commun.* **4,** (2013).
10. Firestone, M. A., Hayden, S. C. & Huber, D. L. Greater than the sum: Synergy and emergent properties in nanoparticle–polymer composites. *MRS Bull.* **40,** 760–767 (2015).
11. Hecht, L. L. *et al.* Influence of the Surfactant Concentration on Miniemulsion Polymerization for the Preparation of Hybrid Nanoparticles. *Macromol. Chem. Phys.* **213,** 2165–2173 (2012).
12. Joumaa, N. *et al.* Synthesis of Quantum Dot-Tagged Submicrometer Polystyrene Particles by Miniemulsion Polymerization. *Langmuir* **22,** 1810–1816 (2006).
13. Luo, Q., Hickey, R. J. & Park, S. Controlling the Location of Nanoparticles in Colloidal Assemblies of Amphiphilic Polymers by Tuning Nanoparticle Surface Chemistry. *ACS Macro Lett.* **2,** 107–111 (2013).
14. Guo, Q. *et al.* Comparison of in Situ and ex Situ Methods for Synthesis of Two-Photon Polymerization Polymer Nanocomposites. *Polymers (Basel).* **6,** 2037–2050 (2014).
15. Bao, C., Jin, M., Lu, R., Zhang, T. & Zhao, Y. Y. Preparation of Au nanoparticles in the presence of low generational poly(amidoamine) dendrimer with surface hydroxyl groups. *Mater. Chem. Phys.* **81,** 160–165 (2003).

16. Xu, Y., Chen, D., Jiao, X. & Xue, K. Nanosized Cu2O/PEG400 Composite Hollow Spheres with Mesoporous Shells. *J. Phys. Chem. C* **111,** 16284–16289 (2007).
17. Zhang, J. *et al.* Facile Methods to Coat Polystyrene and Silica Colloids with Metal. *Adv. Funct. Mater.* **14,** 1089–1096 (2004).
18. Wang, D. & Caruso, F. Polyelectrolyte-coated colloid spheres as templates for sol-gel reactions. *Chem. Mater.* **14,** 1909–1913 (2002).
19. Taubert, A., Palms, D., Weiss, Ö., Piccini, M. T. & Batchelder, D. N. Polymer-assisted control of particle morphology and particle size of zinc oxide precipitated from aqueous solution. *Chem. Mater.* **14,** 2594–2601 (2002).
20. Imai, Y. *et al.* Transparent poly(bisphenol A carbonate)-based nanocomposites with high refractive index nanoparticles. *Eur. Polym. J.* **45,** 630–638 (2009).
21. Guan, C., Lü, C., Cheng, Y., Song, S. & Yang, B. A facile one-pot route to transparent polymer nanocomposites with high ZnS nanophase contents via in situ bulk polymerization. *J. Mater. Chem.* **19,** 617–621 (2009).
22. Ritzhaupt-Kleissl, E., Boehm, J., Hausselt, J. & Hanemann, T. Thermoplastic polymer nanocomposites for applications in optical devices. *Mater. Sci. Eng. C* **26,** 1067–1071 (2006).
23. Kolhatkar, A., Jamison, A., Litvinov, D., Willson, R. & Lee, T. Tuning the Magnetic Properties of Nanoparticles. *Int. J. Mol. Sci.* **14,** 15977–16009 (2013).
24. Akbarzadeh, A., Samiei, M. & Davaran, S. Magnetic nanoparticles: preparation, physical properties, and applications in biomedicine. *Nanoscale Res. Lett.* **7,** 144 (2012).
25. Sung Lee, J., Myung Cha, J., Young Yoon, H., Lee, J.-K. & Keun Kim, Y. Magnetic multi-granule nanoclusters: A model system that exhibits universal size effect of magnetic coercivity. *Sci. Rep.* **5,** 12135 (2015).
26. Schmidt, A. M. The Synthesis of Magnetic Core-Shell Nanoparticles by Surface-Initiated Ring-Opening Polymerization of?-Caprolactone. *Macromol. Rapid Commun.* **26,** 93–97 (2005).
27. Yang, C., Li, H., Xiong, D. & Cao, Z. Hollow polyaniline/Fe3O4 microsphere composites: Preparation, characterization, and applications in microwave absorption. *React. Funct. Polym.* **69,** 137–144 (2009).
28. Chertok, B. *et al.* Iron oxide nanoparticles as a drug delivery vehicle for MRI monitored magnetic targeting of brain tumors. *Biomaterials* **29,** 487–496 (2008).
29. Thierry, B. *et al.* Multifunctional core–shell magnetic cisplatin nanocarriers. *Chem. Commun.* 7348 (2009). doi:10.1039/b911703b
30. Hanemann, T. & Szabó, D. V. Polymer-Nanoparticle Composites: From Synthesis to Modern Applications. *Materials (Basel).* **3,** 3468–3517 (2010).
31. Wang, X.-H., Chen, R.-Z., Gui, Z.-L. & Li, L.-T. The grain size effect on dielectric properties of BaTiO3 based ceramics. *Mater. Sci. Eng. B* **99,** 199–202 (2003).
32. Buscaglia, V. *et al.* Grain size and grain boundary-related effects on the properties of nanocrystalline barium titanate ceramics. *J. Eur. Ceram. Soc.* **26,** 2889–2898 (2006).

33. Xie, S.-H., Zhu, B.-K., Wei, X.-Z., Xu, Z.-K. & Xu, Y.-Y. Polyimide/BaTiO3 composites with controllable dielectric properties. *Compos. Part A Appl. Sci. Manuf.* **36,** 1152–1157 (2005).
34. Schumacher, B., Geßwein, H., Haußelt, J. & Hanemann, T. Temperature treatment of nano-scaled barium titanate filler to improve the dielectric properties of high-k polymer based composites. *Microelectron. Eng.* **87,** 1978–1983 (2010).
35. Pant, H., Patra, M., Verma, A., Vadera, S. & Kumar, N. Study of the dielectric properties of barium titanate–polymer composites. *Acta Mater.* **54,** 3163–3169 (2006).
36. Aricò, A. S., Bruce, P., Scrosati, B., Tarascon, J. & van Schalkwijk, W. Nanostructured materials for advanced energy conversion and storage devices. *Nat. Mater.* **4,** 366–377 (2005).
37. Wang, Y., Lee, J. Y. & Chen, B.-H. Microemulsion Syntheses of Sn and SnO2-Graphite Nanocomposite Anodes for Li-Ion Batteries. *J. Electrochem. Soc.* **151,** A563 (2004).
38. Yao, J., Shen, X., Wang, B., Liu, H. & Wang, G. In situ chemical synthesis of SnO2–graphene nanocomposite as anode materials for lithium-ion batteries. *Electrochem. commun.* **11,** 1849–1852 (2009).
39. Xiao, J. *et al.* Exfoliated MoS 2 Nanocomposite as an Anode Material for Lithium Ion Batteries. *Chem. Mater.* **22,** 4522–4524 (2010).
40. Krawiec, W. *et al.* Polymer nanocomposites: a new strategy for synthesizing solid electrolytes for rechargeable lithium batteries. *J. Power Sources* **54,** 310–315 (1995).
41. Croce, F. Nanocomposite polymer electrolytes and their impact on the lithium battery technology. *Solid State Ionics* **135,** 47–52 (2000).
42. Brinker, C. J. *et al.* Aerosol-assisted self-assembly of mesostructured spherical nanoparticles. *Nature* **398,** 223–226 (1999).
43. Tsung, C. K. *et al.* A general route to diverse mesoporous metal oxide submicrospheres with highly crystalline frameworks. *Angew. Chemie - Int. Ed.* **47,** 8682–8686 (2008).
44. Suh, W. H. & Suslick, K. S. Magnetic and Porous Nanospheres from Ultrasonic Spray Pyrolysis. *J. Am. Chem. Soc.* **127,** 12007–12010 (2005).
45. Kang, H. S., Kang, Y. C., Park, H. D. & Shul, Y. G. Morphology of particles prepared by spray pyrolysis from organic precursor solution. *Mater. Lett.* **57,** 1288–1294 (2003).
46. Kang, H. S. *et al.* Nano-sized ceria particles prepared by spray pyrolysis using polymeric precursor solution. *Mater. Sci. Eng. B* **127,** 99–104 (2006).
47. Ju, S. H. & Kang, Y. C. Fine-sized LiNi0.8Co0.15Mn0.05O2 cathode particles prepared by spray pyrolysis from the polymeric precursor solutions. *Ceram. Int.* **35,** 1633–1639 (2009).
48. Kim, H.-S., Lee, K.-H. & Kim, S.-G. Growth of Monodisperse Silver Nanoparticles in Polymer Matrix by Spray Pyrolysis. *Aerosol Sci. Technol.* **40,** 536–544 (2006).

49. Lee, K. H., Rah, S. C. & Kim, S.-G. Formation of monodisperse silver nanoparticles in poly(vinylpyrrollidone) matrix using spray pyrolysis. *J. Sol-Gel Sci. Technol.* **45,** 187–193 (2008).
50. Tran, Q. H., Nguyen, V. Q. & Le, A.-T. Silver nanoparticles: synthesis, properties, toxicology, applications and perspectives. *Adv. Nat. Sci. Nanosci. Nanotechnol.* **4,** 33001 (2013).
51. Fonseca, F. C. *et al.* Superparamagnetism and magnetic properties of Ni nanoparticles embedded in SiO2. *Phys. Rev. B* **66,** 104406 (2002).
52. Raj, K. & Boulton, R. J. Ferrofluids — Properties and applications. *Mater. Des.* **8,** 233–236 (1987).
53. Chen, C., Kelder, E. M., van der Put, P. J. J. M. & Schoonman, J. Morphology control of thin LiCoO2 films fabricated using the electrostatic spray deposition (ESD) technique. *J. Mater. Chem.* **6,** 765 (1996).
54. Jung, D. S., Park, S. Bin & Kang, Y. C. Design of particles by spray pyrolysis and recent progress in its application. *Korean J. Chem. Eng.* **27,** 1621–1645 (2010).
55. Motl, N. E., Mann, A. K. P. & Skrabalak, S. E. Aerosol-assisted synthesis and assembly of nanoscale building blocks. *J. Mater. Chem. A* **1,** 5193 (2013).
56. Yeh, H.-C. & Liu, B. Y. H. Aerosol filtration by fibrous filters—I. theoretical. *J. Aerosol Sci.* **5,** 191–204 (1974).
57. Yeh, H.-C. & Liu, B. Y. H. Aerosol filtration by fibrous filters—II. experimental. *J. Aerosol Sci.* **5,** 205–217 (1974).
58. Stern, K. H. High Temperature Properties and Decomposition of Inorganic Salts Part 3, Nitrates and Nitrites. *J. Phys. Chem. Ref. Data* **1,** 747–772 (1972).
59. Brockner, W., Ehrhardt, C. & Gjikaj, M. Thermal decomposition of nickel nitrate hexahydrate, Ni(NO3)2·6H2O, in comparison to Co(NO3)2·6H2O and Ca(NO3)2·4H2O. *Thermochim. Acta* **456,** 64–68 (2007).
60. Le Bail, A. Whole powder pattern decomposition methods and applications: A retrospection. *Powder Diffr.* **20,** 316–326 (2005).
61. Patterson, A. L. The Scherrer Formula for X-Ray Particle Size Determination. *Phys. Rev.* **56,** 978–982 (1939).
62. Adhikari, R. & Michler, G. H. Polymer Nanocomposites Characterization by Microscopy. *Polym. Rev.* **49,** 141–180 (2009).
63. Mondini, S., Ferretti, A. M., Puglisi, A. & Ponti, A. Pebbles and PebbleJuggler: software for accurate, unbiased, and fast measurement and analysis of nanoparticle morphology from transmission electron microscopy (TEM) micrographs. *Nanoscale* **4,** 5356 (2012).
64. Schneider, C. A., Rasband, W. S. & Eliceiri, K. W. NIH Image to ImageJ: 25 years of image analysis. *Nat. Methods* **9,** 671–675 (2012).
65. Vrandečić, N. S., Erceg, M., Jakić, M. & Klarić, I. Kinetic analysis of thermal degradation of poly(ethylene glycol) and poly(ethylene oxide)s of different molecular weight. *Thermochim. Acta* **498,** 71–80 (2010).
66. Pielichowski, K. & Flejtuch, K. Non-oxidative thermal degradation of poly(ethylene oxide): kinetic and thermoanalytical study. *J. Anal. Appl. Pyrolysis* **73,** 131–138 (2005).

67. Loría-Bastarrachea, M. I. *et al.* A TG/FTIR study on the thermal degradation of poly(vinyl pyrrolidone). *J. Therm. Anal. Calorim.* **104,** 737–742 (2011).
68. Lee, C. J., Park, J. & Yu, J. A. Catalyst effect on carbon nanotubes synthesized by thermal chemical vapor deposition. *Chem. Phys. Lett.* **360,** 250–255 (2002).
69. Esconjauregui, S., Whelan, C. M. & Maex, K. The reasons why metals catalyze the nucleation and growth of carbon nanotubes and other carbon nanomorphologies. *Carbon N. Y.* **47,** 659–669 (2009).
70. Lin, W.-H. & Li, Y.-Y. Field emission properties of tapered carbon nanotubes synthesized by the pyrolysis of poly(ethylene glycol) using a nickel catalyst. *Diam. Relat. Mater.* **22,** 124–127 (2012).
71. Kitahara, Y., Takahashi, S. & Fujii, T. Thermal analysis of polyethylene glycol: Evolved gas analysis with ion attachment mass spectrometry. *Chemosphere* **88,** 663–669 (2012).
72. Purohit, R., Purohit, K., Rana, S., Rana, R. S. & Patel, V. Carbon Nanotubes and Their Growth Methods. *Procedia Mater. Sci.* **6,** 716–728 (2014).
73. Kumar, M. in *Carbon Nanotubes - Synthesis, Characterization, Applications* (InTech, 2011). doi:10.5772/19331
74. Shenoy, A. V. & Saini, D. R. *Thermoplastic Melt Rheology and Processing*. (Marcel Dekker, Inc., 1996).
75. Hinds, W. C. *Aerosol Technology: Properties, Behavior, and Measurement of Airborne Particles*. (John Wiley & Sons, 1982).
76. Liu, J., Cao, D. & Zhang, L. Molecular Dynamics Study on Nanoparticle Diffusion in Polymer Melts: A Test of the Stokes−Einstein Law. *J. Phys. Chem. C* **112,** 6653–6661 (2008).
77. Brochard Wyart, F. & de Gennes, P. G. Viscosity at small scales in polymer melts. *Eur. Phys. J. E - Soft Matter* **1,** 93–97 (2000).
78. Tuteja, A., Mackay, M. E., Narayanan, S., Asokan, S. & Wong, M. S. Breakdown of the Continuum Stokes−Einstein Relation for Nanoparticle Diffusion. *Nano Lett.* **7,** 1276–1281 (2007).
79. Grabowski, C. a & Mukhopadhyay, A. Size Effect of Nanoparticle Diffusion in a Polymer Melt. *Macromolecules* **47,** 7238–7242 (2014).
80. Friedlander, S. . & Wang, C. . The self-preserving particle size distribution for coagulation by brownian motion. *J. Colloid Interface Sci.* **22,** 126–132 (1966).
81. Friedlander, S. K. & Marlow, W. H. Smoke, Dust and Haze: Fundamentals of Aerosol Behavior. *Phys. Today* **30,** 58–59 (1977).
82. Voorhees, P. W. The theory of Ostwald ripening. *J. Stat. Phys.* **38,** 231–252 (1985).
83. Wunderlich, B. & Kreitmeier, S. N. Defects in Polymer Crystals. *MRS Bull.* **20,** 17–22 (1995).
84. Wunderlich, B. *Thermal Analysis of Polymeric Materials*. (Springer-Verlag, 2005). doi:10.1007/b137476
85. Carné-Sánchez, A., Imaz, I., Cano-Sarabia, M. & Maspoch, D. A spray-drying strategy for synthesis of nanoscale metal–organic frameworks and their assembly into hollow superstructures. *Nat. Chem.* **5,** 203–211 (2013).